The Halo Masses of Galaxies to $z \sim 3$: A Hybrid Observational and Theoretical Approach

Christopher J. Conselice[1,2] , Jonathan W. Twite[1,2], David P. Palamara[4,5], and William Hartley[1,2,3]

[1] Centre for Astronomy and Particle Theory, School of Physics & Astronomy, University of Nottingham, Nottingham, NG7 2RD, UK
[2] University of Nottingham, School of Physics & Astronomy, Nottingham, NG7 2RD, UK
[3] ETH Zurich, Institute for Astronomy, Wolfgang-Pauli-Strasse 27, CH-8093 Zurich, Switzerland
[4] Monash University, School of Physics, Wellington Rd., Clayton, 3800, VIC, Australia
[5] Monash Centre for Astrophysics (MoCA), Wellington Rd., Clayton, 3800, VIC, Australia
Received 2018 March 6; revised 2018 June 4; accepted 2018 June 17; published 2018 August 8

Abstract

We use a hybrid observational/theoretical approach to study the relation between galaxy kinematics and the derived stellar and halo masses of galaxies up to $z = 3$ as a function of stellar mass, redshift, and morphology. Our observational sample consists of a concatenation of 1125 galaxies with kinematic measurements at $0.4 < z < 3$ from long-slit and integral field studies. We investigate several ways to measure halo masses from observations based on results from semi-analytical models, showing that galaxy halo masses can be retrieved with a scatter of ~0.4 dex by using only stellar masses. We discover a third parameter, relating to the time of the formation of the halo, that reduces the scatter in the relation between the stellar and halo masses such that systems forming earlier have a higher stellar mass–to–halo mass ratio, which we also find observationally. We find that this scatter correlates with morphology such that early-type or older stellar systems have higher $M_*/M_{\rm halo}$ ratios. We furthermore show, using this approach and through weak lensing and abundance matching, that the ratio of stellar to halo mass does not significantly evolve with redshift at $1 < z < 3$. This is evidence for the regulated hierarchical assembly of galaxies such that the ratio of stellar to dark matter mass remains approximately constant since $z = 2$. We use these results to show that the dark matter accretion rate evolves from $dM_{\rm halo}/dt \sim 4000\,M_\odot$ yr^{-1} at $z \sim 2.5$ to a few $100\,M_\odot$ yr^{-1} by $z \sim 0.5$.

Key words: dark matter – galaxies: evolution – galaxies: formation

1. Introduction

In the currently favored hierarchical picture of the formation of galaxies, small density fluctuations of matter in the early universe induce the first dark matter halos to collapse (e.g., White & Rees 1978; Davis et al. 1985). Gas later collapses within these halos and eventually cools to form the first stars. At the same time this occurs, these dark matter halos are merging and accreting matter and thereby grow in both dark matter and baryonic content over time. The details of this picture have, however, yet to be worked out, and we are just starting to understand the contribution of various processes responsible for galaxy assembly among many others (e.g., Ownsworth et al. 2014; Mundy et al. 2017).

Dark matter makes up a major portion of the total mass within the universe, yet due to observational constraints, very little is known concerning how dark matter has evolved within galaxies over the history of the universe. Measuring dark matter masses is, however, of fundamental importance to our full understanding of galaxy evolution/formation, since dark matter halos drive their gravitational interactions as galaxies evolve through time (e.g., Conroy & Wechsler 2009; Foucaud et al. 2010; Behroozi et al. 2013; Skibba et al. 2015). Ideally, we would like to be able to trace dark matter and its relationship to individual galaxies as a function of cosmic time, yet this has proven difficult.

On the largest scales, massive dark matter halos hold galaxy groups and clusters together, helping to shape the largest environments in the universe. Predictions for the structure of these largest dark matter "scaffoldings" match well with observations (Springel et al. 2005). However, dark matter on the scales of galaxies is the ultimate way to test our

cosmological ideas, as it is where the very complex interplay between baryons, star formation, and active galactic nuclei (AGNs) all contribute to the structure and evolution of galaxies. Therefore, tracing dark matter within galaxies over cosmic time is an important observational goal, yet one that was until recently not possible to realize in any significant way.

The presence of dark matter within galaxies is ideally inferred from observations of baryonic matter, if possible. The traditional method for measuring the dark matter content of galaxies is through their internal kinematics and using this to derive their so-called dynamical masses. This is, in fact, how dark matter in galaxies was first inferred (e.g., Faber & Gallagher 1979), and it remains the primary method for measuring the amount of dark matter on the scale of galaxies. With the increase in the number of integral field units (IFUs; e.g., SINFONI, KMOS, FLAMES/GIRAFFE) and higher-resolution multi-object long-slit spectrographs (for example, FORS, MOSFIRE, GMOS, and DEEP2) on telescopes, kinematic measures are being obtained for increasing large numbers of high-redshift galaxies (e.g., Pasquini et al. 2002; Eisenhauer et al. 2003; Bonnet et al. 2004; Epinat et al. 2009; Förster Schreiber et al. 2009; Buitrago et al. 2013; Wisnioski et al. 2015; Price et al. 2016; Tiley et al. 2016; Wuyts et al. 2016; Guerou et al. 2017; Ubler et al. 2017). Measuring the dark matter content with kinematics for large numbers of individual galaxies at redshifts beyond $z \sim 3$ is, however, still very difficult using current technological capabilities. Furthermore, the observed kinematics of these observations only probes the inner parts of galaxies and often does not reveal the total or halo masses of galaxies.

On the other hand, stellar masses are the most easily accessible type of mass in galaxies to measure, and there has been a considerable amount of work measuring stellar masses for galaxies at both low and high redshift up to $z \sim 10$ (e.g., Bell et al. 2003; Bundy et al. 2006; Mortlock et al. 2011; Duncan et al. 2014). Stellar masses (M_*) of galaxies are usually calculated from multiwavelength observations (for example, Bundy et al. 2006; Mortlock et al. 2011). Stellar mass functions and stellar mass comoving volume densities have now been studied in detail, indicating a clear history of stellar mass growth, whereby around half of all stellar mass is in place by $z \sim 1$ (e.g., Drory et al. 2005; Conselice et al. 2007; Elsner et al. 2008; Pérez-González et al. 2008; Mortlock et al. 2011, 2015; Ilbert et al. 2013; Muzzin et al. 2013; Duncan et al. 2014).

In this paper, we provide a detailed investigation of how stellar and dark matter masses can be measured up to $z \sim 3$ in a systematic way on individual systems. We investigate different methods of measuring the dynamical and halo masses of galaxies through kinematics and abundance matching. While measuring the masses of distant galaxies is now done using methods such as clustering, weak lensing, and abundance matching, these methods are all statistical in nature and cannot easily be used to predict the halo masses of individual galaxies. We describe whether and how these masses agree with each other at high redshift and discuss evidence for any evolution. We furthermore use these techniques and results to determine the accretion rate of dark matter into galaxies at $z < 1.2$ and compare with theoretical models. By measuring the dark matter masses of individual galaxies, we may be better able to directly use galaxy evolution to test fundamental features of the universe, such as dark matter and cosmological parameters, as well as better connect simulated dark matter halos with observations (e.g., Conselice 2014).

As such, we present a new approach to tracing dark matter in galaxies that relies on theoretical models. This is not ideal, as we would naturally want a purely observational method. However, using a model is necessary to obtain the dark halo masses for other methods as well, including through clustering and abundance matching. Furthermore, often simple equations relating the size and velocity are used to measure the dark matter of distant galaxies, yet these simple relations have not yet been tested. We carry out an examination of these issues in this paper and discuss the implications for galaxy formation.

In the first part of this paper, we measure the different types of masses (stellar, dynamical, and halo matter mass, hereafter M_{halo}) for a sample of 432 galaxies from the DEEP2 survey supplemented by other samples (Section 2). We furthermore describe how to measure different masses for these galaxies, namely the stellar mass (M_*), dynamical mass (M_{dyn}), and total halo mass (M_{halo}), in Section 3. Then, in Section 4, we use these to derive relationships between M_* and M_{halo} and how these evolve between redshifts. In essence, this paper's conclusions are divided into theoretical results in Section 3 and observational results in Section 4. In Section 5, we discuss our results in their entirety, the limitations inherent in our method, and what future work is needed to make progress in this direction, while Section 6 is a summary.

Throughout the paper, we adopt the cosmology $\Omega_m = 0.3$, $\Omega_\Lambda = 0.7$, and $H_0 = 70 \, km \, s^{-1} \, Mpc^{-1}$. For all masses and star formation rates (SFRs), we use a Chabrier initial mass function (IMF; Chabrier 2003), converting masses using other IMFs, if necessary, in order to compare with other work.

2. Data and Sample

2.1. Sample Overview

In this section, we describe the several samples of galaxies we use in this paper. The data we use are all previously published. Our primary sample, in which we establish the relationship between stellar and dark matter masses up to $z \sim 1.2$, is from the Palomar Observatory Wide-field IR (POWIR) overlap with the DEEP2 survey (e.g., Davis et al. 2003; Conselice et al. 2008a).

We furthermore utilize stellar masses and derived dynamical masses from studies such as Conselice et al. (2005), Treu et al. (2005), Erb et al. (2006), Förster Scheiber et al. (2009), Epinat et al. (2009), Buitrago et al. (2013), Beifiori et al. (2014), and Price et al. (2016) in what we call our secondary samples. We describe these different samples and their uses and limitations below.

2.2. Primary Sample

We use as our primary sample galaxies within the POWIR/DEEP2 survey (e.g., Davis et al. 2003; Kassin et al. 2007; Conselice et al. 2008a) for which kinematic measurements, stellar masses, measured SFRs, and resolved sizes from *Hubble Space Telescope* (*HST*) imaging are available. The DEEP2 survey is a 2.3 deg^2 area spectroscopic survey with galaxy selection done in magnitude and color. The spectroscopy for DEEP2 was taken with the DEIMOS spectrograph, spanned the range 6100–9100 Å, and was carried out with the 1200 line mm^{-1} grating, providing a high enough resolution that internal kinematics can be measured. However, for this study, we only use data in the extended Groth strip (EGS) field where deep *HST* and stellar mass information is available as part of the AEGIS survey (e.g., Davis et al. 2007; Conselice et al. 2008a).

The POWIR/DEEP2 primary sample spans a wide range in redshift, stellar mass, star formation, morphology, and color. Using a redshift limit of $z = 1.2$, however, biases the galaxies toward those with some star formation. Our sample is selected based on an emission-line cut with integrated intensities $>1500 \, e^- \, Å^{-1}$ in the summed one-dimensional spectrum. The final sample after additional checks and cuts (see also Kassin et al. 2007) consists of 544 galaxies primarily selected on emission-line strength that are not AGNs. In order to use the measured kinematics to derive further information, we discard galaxies that have velocity dispersions less than $\sim 10 \, km \, s^{-1}$ or rotational velocities less than $\sim 5 \, km \, s^{-1}$. This leaves 432 primary sample galaxies in total in which we investigate relationships between different types of masses. We show the primary sample's stellar mass distribution with redshift in Figure 1.

The DEEP2 primary galaxies fall within the POWIR survey (Conselice et al. 2007, 2008a), a large-area ($\sim 1.5 \, deg^2$) deep NIR survey in the K and J bands incorporating multiwavelength and spectroscopic data from other telescopes, such as the CFHT, *GALEX*, *Spitzer*, and *Chandra* (Davis et al. 2007; Conselice et al. 2008a). We utilize the stellar mass catalog from Conselice et al. (2007) to obtain the stellar masses of these galaxies from the spectral energy distribution (SED) fitting as described in Bundy et al. (2006).

We furthermore also use single-orbit images from the *HST* Advanced Camera for Surveys (ACS) in the F606W (V) and
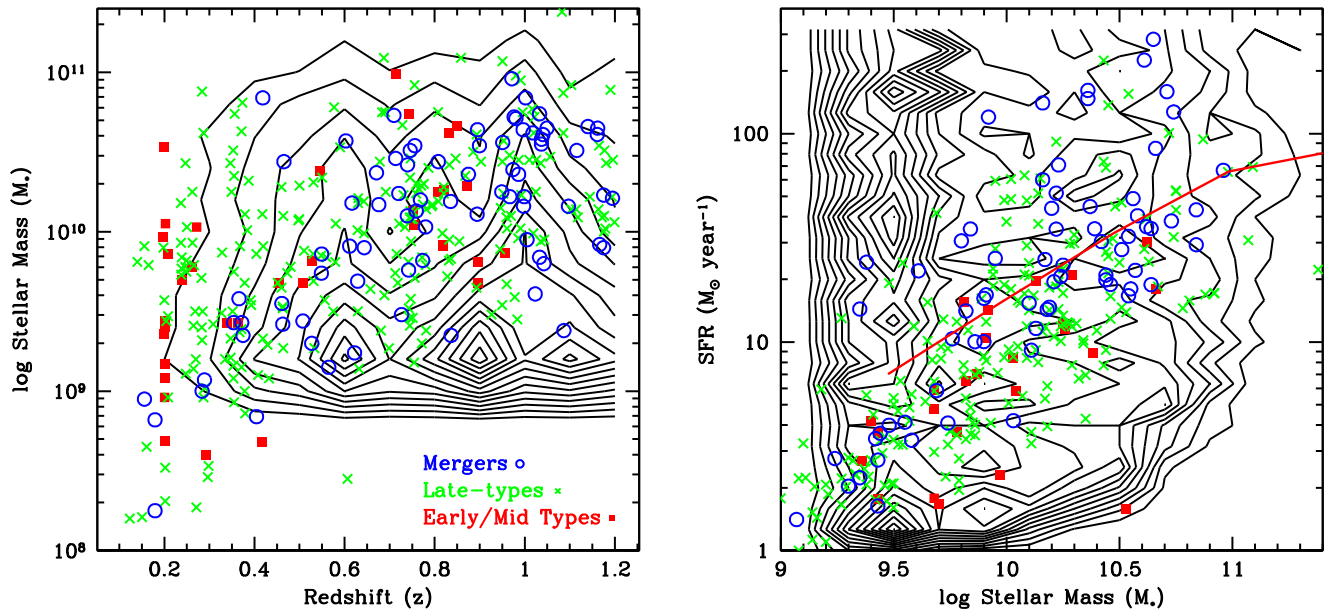
Figure 1. Plot on the left shows the stellar mass distribution as a function of redshift for our primary sample in reference to a field galaxy sample down to a depth of $K = 26$ AB. The right panel shows the SFR vs. stellar mass diagram. Shown as the colored points are the galaxies in our primary sample of DEEP2/POWIR galaxies that we use throughout this paper. The contours are a sample of the Ultra Deep Survey sample galaxies taken from the analysis of Mortlock et al. (2015). The solid red line in the right panel is the main sequence of star formation at $z = 1.5$ from Bauer et al. (2011). The primary sample points are coded by the morphological type of each galaxy.

F814W (I) bandpasses to classify these DEEP2-selected galaxies into morphological types through an automated morphological classification through the CAS method (Conselice 2003). The details of how the CAS measurements are done are described in Conselice (2003), Conselice et al. (2008a), and Twite et al. (2012). When we classify our galaxies, we find that there is a mixture of types from ellipticals, to disks, to irregulars/mergers within our sample. The definitions for each morphological class are taken from Conselice et al. (2008b) and summarized in Table 1.

Quantitatively, our primary sample is composed of seven (2%) early types, 36 (8%) mid-types, 290 (67%) late types, and 99 (23%) merging galaxies. This is not representative of nearby galaxy types but is closer to what one finds at higher redshifts, where galaxies are almost all star-forming (e.g., Mortlock et al. 2013). However, the morphologies of these galaxies are not a significant part of our analysis, and we only use this aspect to test how morphology may affect the results we find. Different morphologies are important when we examine the secondary sample later in the paper and are selected by morphological type (i.e., disk or elliptical) or through stellar mass.

The galaxies in this primary DEEP2/POWIR survey have SFRs derived from UV measurements from *GALEX* (Schiminovich et al. 2007, which also contains details on how the correction for dust attenuation was calculated) and/or IR measurements from *Spitzer* 24 μm data (Noeske et al. 2007). Among this sample, 379 galaxies have a UV-derived SFR, and we use these values as an indicator of the SFR. Another 23 only have IR-derived SFRs that are used; 30 galaxies have no SFR measurement.

It is important to note that our primary sample is biased in that we do not explore the entire galaxy population with a balanced mixture of morphologies, masses, and SFRs. However, our sample is representative of all galaxy types that exist

Table 1
CAS Parameters for Morphological Classifications for
Our Primary DEEP2/POWIR Sample

Morphological Type	CAS Parameters	Number
Early-type galaxies	$C > 21.5 \log_{10}(A) + 31.2$	7
Mid-type galaxies	$C < 21.5 \log_{10}(A) + 31.2$ and $C > 2.44 \log_{10}(A) + 5.49$ and $A < 0.35$	36
Late-type galaxies	$C < 2.44 \log_{10}(A) + 5.49$ and $A < 0.35$	290
Merging galaxies	$A > 0.35$	99

Note. Also shown is the number of galaxies within each classification bin.

at $z < 1$ (Figure 1), with the exception of truly passive galaxies with no emission lines.

We show this by examining where our primary sample falls in the three-dimensional space of redshift, stellar mass, and SFR for a stellar mass–selected sample (Figure 1). These properties are taken from the Ultra Deep Survey (Mortlock et al. 2015) selected by $z < 1.2$ and using a $K = 26$ mag limit. As can be seen by the contours, we are primarily missing out on very low mass galaxies and passive systems without star formation. Therefore, any conclusions we draw in this paper based only on the primary sample are necessarily restricted to higher-mass galaxies with some star formation. However, we supplement this sample with a broad range of galaxy types (Section 2.3). Note from Figure 1 that we do include galaxies with quite low SFRs, although not at the highest masses. However, we investigate these elliptical systems through our supplemental sample from Treu et al. (2005) and Beifiori et al. (2014; Section 2.3) and other secondary sources.

The effective radii (R_e) and Sérsic index of the primary sample were measured by Conselice et al. (2008a) and Trujillo et al. (2007) from the *HST*/ACS F814W-band imaging of the POWIR EGS field.

2.3. Secondary Samples

In our larger kinematic secondary sample, we use extensive data from various previous studies. These samples do not contain all the ingredients of the primary sample—kinematics, morphologies, sizes, SFRs, etc.—so we only use them in a limited way to test how the results derived from the primary sample apply. The samples we use are Conselice et al. (2005), Treu et al. (2005), Erb et al. (2006), Epinat et al. (2009), Förster Schreiber et al. (2009), Miller et al. (2011, 2014), Buitrago et al. (2013), Beifiori et al. (2014), and Price et al. (2016).

Part of this includes 257,000 galaxies from the BOSS survey that are mostly massive early types (Beifiori et al. 2014). These are samples where there are at least kinematic and stellar mass measurements for galaxies at $z > 0.2$. This is not an exhaustive list of studies using internal kinematic data at high redshift, but it is representative of the different types of galaxies that have been observed kinematically beyond the local universe. These secondary samples are often missing another component of information that we have in our primary sample. This includes *HST* imaging for sizes, or accurate SFRs, which limits our ability to obtain accurate dynamical masses as we can for the primary sample.

We give a brief summary of these samples here. Conselice et al. (2005) measured the kinematics of 101 galaxies at $0.2 < z < 1.2$ whose morphologies are disk-like. A similar study by Miller et al. (2011, 2014) measures rotation curves for 129 disk-like galaxies at the same redshifts. On the other hand, Treu et al. (2005) measured internal velocity dispersions of 165 elliptical and spheroidal galaxies at redshifts similar to those in these disk studies. These are in contrast to the DEEP2 sample, which is not selected by any particular morphological type.

For galaxies at the highest redshifts, we use results from studies by Epinat et al. (2009) and Förster Schreiber et al. (2009), who measured kinematics with integral field spectroscopy, and Erb et al. (2006) and Price et al. (2016), who used long-slit spectra. The Erb et al. (2006) sample consists of 114 UV-selected galaxies at $z \sim 2$ whose internal kinematics are measured with deep NIR long-slit spectroscopy. The sample of Förster Schreiber et al. (2009) consists of 62 UV-selected star-forming galaxies at redshifts $1.3 < z < 2.6$ whose internal kinematics are measured with near-infrared IFUs. Buitrago et al. (2013) measured kinematics for 10 very massive galaxies with $M_* > 10^{11} M_\odot$ at $z \sim 1.4$ using SINFONI on the VLT. The Buitrago et al. (2013) galaxies are not selected by SFR or UV flux but by their high stellar masses. The Epinat et al. (2009) sample consists of IFU kinematics for nine emission-line galaxies also measured with SINFONI. Finally, a more recent study of $z \sim 2$ galaxies with MOSFIRE on Keck contains a sample of 178 star-forming galaxies (e.g., Kriek et al. 2015; Price et al. 2016).

Occasionally within these samples, the value of either the maximum velocity or the internal velocity dispersion is not available. Usually this is the case when disk galaxies have no internal velocity dispersion measured or ellipticals have no rotational velocity. We infer the missing values for these by using the average value at a given stellar mass of the missing quantity for galaxies of similar morphology. This is not needed for the majority of our sample, and our ultimate results do not depend on the exact replacement value used.

Details of these observations can be obtained through their respective papers. It is important to point out that these samples were selected by a given property, usually morphology, or by having a high SFR. They are generally not representative of the galaxy population as a whole at their respective redshifts, nor are they homogeneous in terms of stellar masses.

2.4. Alternative Dark Mass Comparison Studies

One of the major goals of this paper is to investigate methods for measuring the dark matter halo masses of galaxies at $z > 1$. Measuring the halo masses of galaxies today is, however, not usually done through kinematics for high-redshift galaxies. In fact, the most common way in which dark masses are measured is as a function of some property, usually stellar mass, that is sometimes further divided into color. The halo masses of these samples are then measured through either clustering (e.g., Foucaud et al. 2010; McCracken et al. 2015; Skibba et al. 2015), lensing (e.g., Leauthaud et al. 2012), or, more recently, abundance matching (e.g., Conroy et al. 2006; Behroozi et al. 2013).

We compare our results with other studies that directly relate the stellar mass to the halo mass. This includes using multi-epoch abundance matching (MEAM) from Moster et al. (2013). We also examine galaxy–galaxy weak lensing of galaxies from Leauthaud et al. (2012). We furthermore use the weak-lensing results from van Uitert et al. (2016). For clustering, we show the Foucaud et al. (2010) results comparing derived halo masses with stellar mass for stellar mass–selected samples. These results are, however, averages for galaxies of a given type or stellar mass and are not individual measures, as is potentially given by kinematic and size measurements. We also compare our results of how halo and stellar masses relate with the same predictions from simulations (Springel et al. 2005; De Lucia & Blaizot 2007; Benson 2012; Section 4).

We discuss in more detail an alternative approach toward understanding the relationship between stellar and halo mass in Section 4.4 using abundance-matching techniques, which is becoming a popular method of tracing the stellar and halo mass evolution of galaxies.

3. Observationally Derived Masses

In this section, we explain how our various masses are measured for our primary and secondary samples, including how we measure their uncertainties. Later, in Section 4, we investigate the halo masses of individual galaxies at high redshift without the use of strong gravitational lensing or other direct ways to measure the halo masses of galaxies. A list of the masses we use and in what section of the paper they are defined and discussed is given in Table 2. In Section 4, we discuss masses that we derive using a hybrid of these observations and theory.

3.1. Stellar Masses

The stellar masses of our primary DEEP2 sample galaxies are calculated in Bundy et al. (2006) and Conselice et al. (2007, 2008a) using targets with high-quality spectroscopic or photometric redshifts from DEEP2 and multiwavelength photometry. These masses are measured using a grid of 13,440 synthetic SEDs from Bruzual & Charlot (2003) spanning a range of exponential star formation histories, ages, metallicities, and dust content. These models are then fit to the photometry for each galaxy to obtain a measure of stellar masses and other stellar population properties. The stellar mass

Table 2
The Definitions of Various Masses Used throughout This Paper

Mass Type	Symbol	Equation	Section
Stellar	M_*	Derived	Section 3.1
Dynamical	$M_{\rm dyn}$	$\dfrac{S_{0.5}^2 r_e}{G}$	Section 3.2
β, dynamical	$M_{\beta,\rm dyn}$	$\dfrac{\beta S_{0.5}^2 r_e}{G}$	Section 3.2
Halo	$M_{\rm halo}$	$a \times (\log {\rm M}_*^b + c)$	Section 4.1
Halo virial	$M_{\rm halo,vir}$	$\dfrac{V_{\rm halo}^2 r_{\rm halo}}{G}$	Section 4.2
Circular	$M_{\rm circ}$	$\dfrac{V_{\rm circ}^2 r_{1/2}}{G}$	Section 4.3.2
Sigma (σ)	$M_{\rm sig}$	$\dfrac{\sigma^2 r_e}{G}$	Section 4.3.3

Note. The sections in which these masses are defined and explained are also listed. Note that our definition of some of these terms, especially dynamical mass, differs from that of previous works (see text).

is determined by scaling the model M_*/L_k ratio to the measured K-band luminosity, L_k.

The details of these masses are explained in Bundy et al. (2006) and Conselice et al. (2007, 2008a), including the uncertainties. While it is hard to pin down the total systematic errors on the measurements of the stellar masses, we have some idea based on the distribution of possible masses from different star formation histories. The typical total error is around 0.2 dex on these measurements. We also examine how TP-AGB stars would change our measured masses and find that the differences for our systems are very low, around 7% on average (Conselice et al. 2007).

For the same galaxies in our primary sample, we also calculate the stellar mass surface density as $\Sigma_* = M_*/\pi R_e^2$ from radius measurements described in Trujillo et al. (2007). We later use these surface densities to determine how density relates to kinematic properties and the halo masses of our sample.

3.2. Dynamical Masses

In this section, we discuss how we measure the dynamical masses of our galaxy samples. This is an important question, and it is not necessarily a well-defined one. Traditionally, the dynamical mass gives some measure of the dark matter mass within a galaxy. However, it is not obvious from an observational perspective how a galaxy's halo mass can be measured.

We therefore divide our dark masses into two types: dynamical masses, which are roughly the total mass of the galaxy within the observed portion of the galaxy, which we discuss in this section, and the total halo mass, which must be derived based on inferring it from observables (Section 4.1). In this section, we only discuss observationally how to obtain a dynamical mass from observables—namely, the size and internal velocities of galaxies.

Note that there are many ways to measure a "dynamical" or "kinematic" mass for galaxies. What we employ here is a method that is meant to be a measure of some fraction of the total or halo mass but is not a total accounting for it. In other words, what we use and define as a dynamical mass is a kinematic indicator that scales with the halo mass, an idea we test later in the paper. This dynamical mass by itself does not

reveal what the total or dark matter mass for galaxies is, and it has to be interpreted alongside the models by which its usefulness is derived.

We measure this dynamical mass by first calculating a total "kinematic" indicator (S_K) for galaxies in our primary sample. The value $S_K = K \times V_{\rm rot}^2 + \sigma_g^2$ (Weiner et al. 2006; Kassin et al. 2007) is a quantity that combines measures of dynamical support from ordered motion with those from disordered motion by combining a factor for the maximal rotational velocity with the velocity dispersion of a galaxy. The value of K depends on the structure of the galaxy, whereby for systems that are spherically symmetric and have an isotropic velocity dispersion with a density that declines as $\sim 1/r^\alpha$, then $\sigma = V_{\rm rot}/\alpha^{1/2} = K^{1/2} \times V_{\rm rot}$. The value $K = 0.5$ is a good compromise for a variety of values with the effective results unchanged if we use another slightly different value. Assuming the quantities measured from the baryonic components of a galaxy trace the underlying total mass, this parameter is calculated for each galaxy in our primary and secondary samples as

$$S_{0.5}^2 = 0.5 V_{\rm rot}^2 + \sigma_g^2. \tag{1}$$

This quantity approximates the global internal kinematics of the galaxy halo system (e.g., Binney & Tremaine 1987). This does, however, imply that certain assumptions must hold—the system should be virialized and symmetric and have an isotropic velocity dispersion and inverse power-law mass density distribution. As much as possible, we use the velocity dispersion measurements at the same radius as the maximum velocity, both of which are corrected for the effects of seeing (e.g., Conselice et al. 2005; Kassin et al. 2007).

Although these assumptions could be considered approximately true for noninteracting galaxies, they would appear to be broken for disturbed and merging systems. Kassin et al. (2007), however, showed that when using the $S_{0.5}$ parameter to build stellar mass Tully–Fisher relations (M_* TFR), the use of $S_{0.5}$ instead of $V_{\rm max}$ has a significant effect on disturbed or compact galaxies and major mergers, bringing them onto the same TFR as other galaxies. Combining these two kinematic properties together into the $S_{0.5}$ index can be interpreted as a measure of the underlying dynamical mass. We discuss this in more detail in the Appendix and Section 5.1.1. This implies that the $S_{0.5}$ versus stellar mass TFR is a more fundamental relationship linking the stellar mass to galaxy dynamics compared to the $V_{\rm rot}$ stellar mass TFR (Section 5.1.1).

Assuming that the halo mass can be correctly measured from the velocity dispersion of a virialized system, this improvement of the TFR implies that we can use the values of $S_{0.5}$ to measure the dynamical masses of virialized systems (we investigate this in more detail in Section 5 and the Appendix). One potential issue is that we are using the velocity dispersion as measured from the kinematics of the gas rather than the stars. However, as has been shown by, e.g., Kobulnicky & Gebhardt (2000), there is a strong correlation between these two quantities. Furthermore, as there is a strong, low-scatter correlation between $S_{0.5}$ and stellar mass (e.g., Kassin et al. 2007; Section 5.1.2), this suggests that the kinematics of the gas is tracing the underlying dynamical properties. Thus, as nonvirialized systems obey the same TFR, we can likely derive their dynamical masses in a similar way.

The dynamical mass is then calculated using the $S_{0.5}$ values for our primary and secondary samples as

$$M_{\rm dyn}(r_e) = \frac{S_{0.5}^2 r_e}{G}. \tag{2}$$

Furthermore, we use the $S_{0.5}$ index to measure the effective velocity dispersion, which differs slightly from previous work. For systems that are pure spheroids with little or no rotation, the value of $S_{0.5}$ is nearly or exactly identical to using the velocity dispersion. For systems that are pure rotational velocity systems, the value of the dynamical mass is as if it were being measured using simple kinematics and measuring the mass content within a fraction of a scale length.

This closely relates to other measures of dynamical masses used in the past (e.g., Conselice et al. 2005; Treu et al. 2005) but in effect uses both the rotational and internal kinematics, while previous examinations have used one or the other. If we were to calculate the total amount of mass in a galaxy, then we would use a coefficient in front of Equation (3) with typical values between 2 and 5 (e.g., Binney & Tremaine 1987). However, as described above, we are using this definition of the dynamical mass in its basic form without any interpretation of what mass it is measuring, as this can vary with the type of galaxy. Ultimately, we are interested in relating this quantity to the total or halo masses of galaxies.

We also calculate at certain times in this paper what we call the dynamical β mass, which is also calculated using the $S_{0.5}$ values as

$$M_{\beta,\rm dyn}(r_e) = \frac{\beta(n) \times S_{0.5}^2 r_e}{G}, \tag{3}$$

where the value of β depends on the Sérsic index, n, in the following way (Cappellari et al. 2006),

$$\beta(n) = 8.87 - 0.831 \times n + 0.0241 \times n^2, \tag{4}$$

where we have used the fitted Sérsic profiles for our galaxies based on surface brightness fits (e.g., Trujillo et al. 2007). Note that although Sérsic fits do not represent the total light distribution in merging galaxies, they are still able to represent the broad light profiles of these systems. The value of β varies between $\beta \sim 6$ for $n = 4$ and $\beta \sim 8.1$ for galaxies with Sérsic indices $n = 1$. We explore how changes to this index would alter our results but find in general that using a canonical value of $\beta = 5$ would not change our results in any significant way. This closely relates to other measures of dynamical masses used in the past but in effect uses both the rotational and internal kinematics, while previous examinations have used one or the other.

4. Measuring Total Halo Masses

In this section, we describe our derived methods for measuring the halo masses of galaxies from observations and theory/models, namely the stellar mass and/or the internal velocities and sizes of individual galaxies, and through abundance matching. Ultimately, we use theoretical models that relate observables to halo mass. We also discuss how similar different mass measures are when compared with each other.

Galaxies reside within dark halos with physical extents that are much larger than their visual radius (e.g., Navarro et al. 1996;

Persic et al. 1996; Cappellari 2006; Kratsov 2013), and measuring the total dark halo masses (hereafter referred to simply as the halo mass) of galaxies is a nontrivial exercise. One can do this to some degree in the local universe by measuring H I velocity rotation curves to a large radius, but there are very few distant galaxies that have such measurements. Likewise, it is possible to use strong gravitational lensing to measure galaxy masses, but the examples of this are rare. It is not clear if these galaxies have especially concentrated light profiles and thus would not be representative of galaxies in general. Furthermore, lensing can only be used in a very small number of systems, but we are interested in a more generalized method for finding the halo masses of individual galaxies.

We therefore must resort to other methods that utilize empirical and model calculations for how halo mass relates to observable properties. This includes using rotation curves, internal velocity dispersions, galaxy abundance matching, and clustering, which can all give measures of average halo masses for a selected population (for example, Conselice et al. 2005; Weinmann et al. 2006; Epinat et al. 2009; Foucaud et al. 2010; Wake et al. 2011; Leauthaud et al. 2012).

Since measuring the halo mass is an important issue, we describe in some detail how we estimate this quantity and describe the uncertainties associated with these inferences. We first discuss how the stellar and halo masses relate for galaxies in simulations as a new approach for obtaining the halo masses of systems. We also check to see how similar the results of this method are in comparison with other methods of obtaining halo masses.

We first describe a model method for measuring the halo mass through relating the observable stellar mass to the halo mass based on simulation output. We then describe a galaxy abundance-matching technique that relates halo mass directly to the observed galaxy stellar mass function using our own measured stellar masses. We finally describe how these measures relate to the ratio of stellar and halo masses derived through clustering. By using and comparing several methods to obtain the halo mass, we quantify how well any one technique may be doing and the systematics that may be present.

4.1. Halo Masses from Stellar Masses Using Models

We present a new way to calculate halo masses from observations by using a semi-empirical/semi-analytical method similar in spirit to that used by Conselice et al. (2005) to calculate the $M_{\rm halo}$ values from $M_{\rm dyn}$. Previously, Conselice et al. (2005) fit the ratio of $M_{\rm halo}$ to $M_{\rm dyn}$ as a function of $M_{\rm dyn}$ from semi-analytical models where both $M_{\rm dyn}$ and $M_{\rm halo}$ are predicted. We investigate this in two ways: by measuring halo masses from stellar masses and later by using kinematics (Section 4.3).

We thus investigate the relationship between the values of M_*, as defined in Section 2, and the halo mass, as found in the semi-analytical models of De Lucia & Blaizot (2007) and the Galacticus simulation from Benson (2014). These are both semi-analytical models that use similar methods and merger trees, but the details of how the astrophysics is included differ. The details of Galacticus can be found in Benson (2014), but we summarize them here for completeness. Galacticus is similar to other semi-analytical codes, such as the one by De Lucia & Blaizot (2007), but is more flexible and adaptable to different input conditions and parameters. In Galacticus, star formation occurs when gas is accreted from the intergalactic
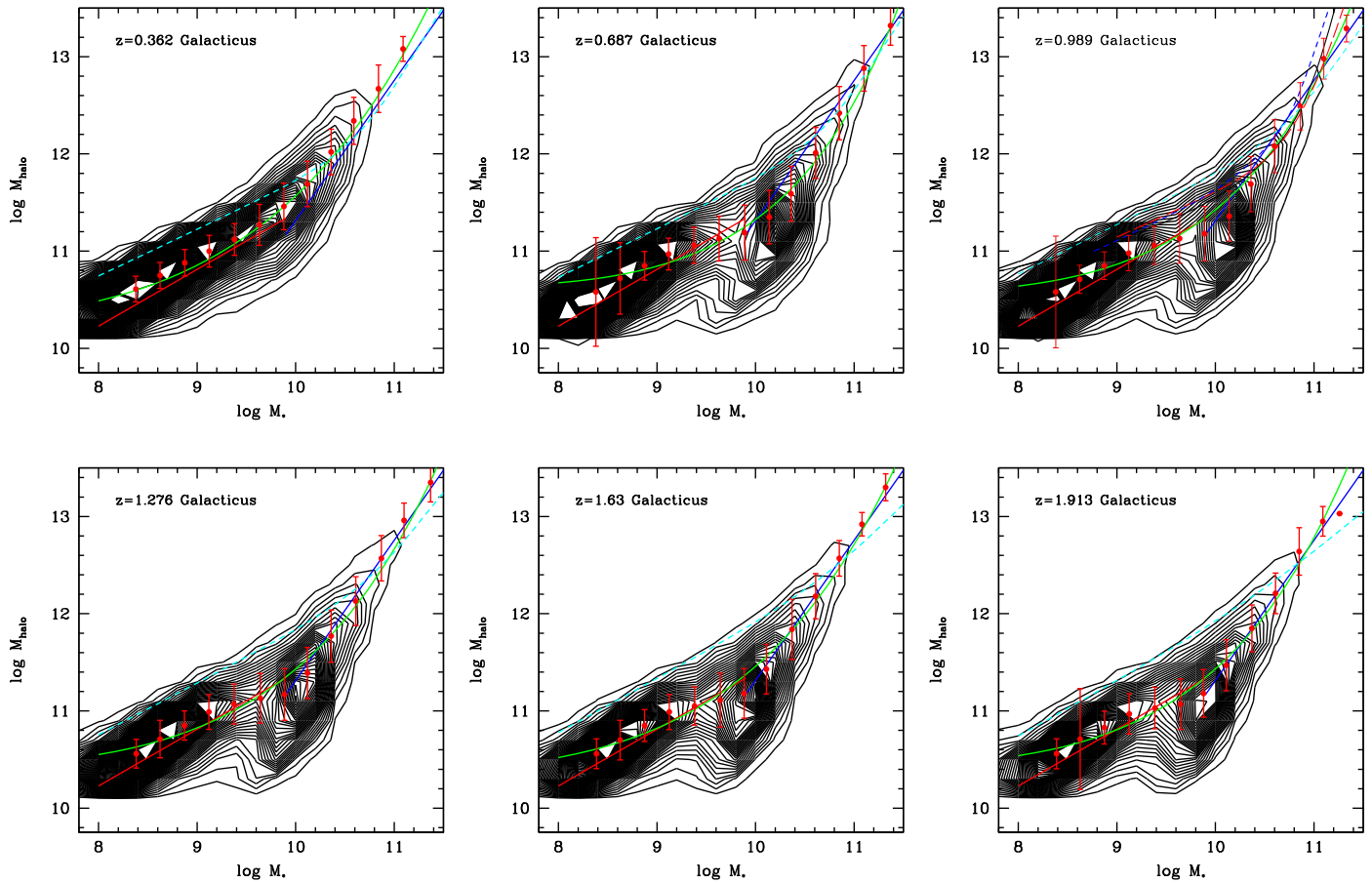
Figure 2. Relation between the stellar mass and halo mass for galaxies within the Galacticus simulation results from Benson (2012). Shown here as the contour plot are the results for these models. The green line shows the best fit to the Galacticus relations, while the red points are the averages of the models at different stellar masses and their 1σ dispersions. The red and blue lines show the fit when using linear relations, with a break at $\log M_* \sim 9.6$. Note that there is very little evolution in terms of the stellar and halo masses as a function of redshift up to $z \sim 2$. We compare our results with empirical measurements from clustering and lensing in the $z = 0.989$ panel. The black curved line is the relationship between stellar and halo mass from the weak-lensing analysis of van Uitert et al. (2016), the red curved line is from the lensing results of Leauthaud et al. (2012), and the blue dashed line is from Moster et al. (2013). The SHAM model of Rodríguez-Puebla et al. (2017) is shown as a cyan dashed line.

medium at a rate that is proportional to the growth rate of the halo. Both models have standard prescriptions for feedback, star formation, and cooling of gas. The Galacticus input is a simplified model of galaxy formation designed to match observations in the local universe, including the galaxy stellar mass function. We carry this comparison out for all stellar masses and thus investigate how this relationship changes as a function of the input stellar mass.

The halo masses in the simulations we use are virial masses, defined as where the density is 200 times the critical density, such that $M_{\mathrm{halo}} = M_{200} = (4\pi/3) \times 200\rho_{\mathrm{critical}}(z)\,R_{200}^3$. Specifically, in Galacticus, the virial mass is defined in the same manner as used in Bryan & Norman (1998), where the density contrast is utilized, implying that it is equal to the virial density assuming a spherical collapse model. To address this, we first use the results of the Galacticus semi-analytical model (Benson 2012) to determine how the relationship between stellar mass and halo mass evolves with time.

We show how the stellar mass changes with halo mass in Galacticus from $z \sim 0.3$ to $z \sim 2$ in Figure 2. As can be seen, there is a change in slope in the correlation between the stellar and halo mass at around $M_* \sim 10^{10}\,M_\odot$. We find that we can fit this relation as either two straight lines (see Appendix) with a break at this stellar mass or as a power law in log space as

given by

$$\log M_{\mathrm{halo}} = a \times (\log M_*)^b + c, \qquad (5)$$

where the best fits for these values are shown in Figure 2 as green solid lines. An important component of this relation is not just the best fit but also the scatter in the values. The red error bars in Figure 2 show the scatter in the relation between the stellar mass and halo mass at these various redshifts. We further discuss this scatter and how it can be minimized in the next section. We also compare with other results relating the stellar mass to halo mass relation, including the relations published in Rodríguez-Puebla et al. (2017), who used subhalo abundance matching (SHAM) to retrieve their relations between stellar and halo masses. We find some differences with this model, particularly at the lowest masses, which is likely an indication that there are subhalo masses being confused with larger host halo masses.

We calculate that the scatter in this fit varies between 0.13 dex for systems at $\log M_* = 9$ and 0.37 at around $\log M_* \sim 11$ in both the Galacticus and Millennium simulations. Table 3 shows the coefficients of this relation at different redshifts.

Table 3
The Fitted Values for Equation (5), which Relates the Stellar Mass and Halo
Mass for Galaxies from the Galacticus Simulation (Section 4.1)

Redshift	a	b	c
0.40	$1.39 \pm 0.23 \times 10^{-7}$	6.99 ± 0.5	10.2 ± 0.1
0.70	$3.89 \pm 0.63 \times 10^{-11}$	10.3 ± 1.1	10.6 ± 0.1
1.00	$4.09 \pm 0.63 \times 10^{-8}$	9.3 ± 1.2	10.5 ± 0.1
1.30	$7.61 \pm 0.16 \times 10^{-7}$	8.1 ± 1.1	10.4 ± 0.2
1.60	$1.89 \pm 0.71 \times 10^{-7}$	7.8 ± 1.2	10.3 ± 0.2
1.90	$2.08 \pm 0.87 \times 10^{-8}$	8.7 ± 1.1	10.4 ± 0.1

This implies that by just using Equation (5), one can, if these models are correct, obtain measurements of the halo mass from the stellar mass within a factor of 2.5 or better, which is slightly larger than the typical uncertainty on stellar mass measurements themselves (e.g., Mortlock et al. 2011, 2015). As we discuss in Section 4.2, significant physics is present within this scatter, with a difference seen between red and blue central galaxies at the higher-mass end of this range (e.g., Rodríguez-Puebla et al. 2015). Furthermore, as we also later find, Rodríguez-Puebla et al. (2015) reported that the scatter increases at higher masses, largely due to a higher differential in formation histories between red and blue centrals.

There are several uncertainties in measuring the halo mass via this method, some of which are discussed in Conselice et al. (2005). One major issue is halo occupation, such that more than one galaxy is in a single halo (e.g., Berlind et al. 2003). However, our relation is derived for individual subhalo and galaxy masses, not the overall larger halo in which it may exist. This limits our ability to compare with results that measure the halo mass of a given sample, as is done through, e.g., clustering or lensing. This is particularly the case for lower-mass systems that are likely within more massive overall halos. Furthermore, these galaxy halo masses are only expected to be accurate to a factor of a few, given the scatter in the relation. There are, however, potential systematics that we investigate by comparing our results to those that are obtained through other methods.

4.2. Third Parameter Effect

One of the major questions in trying to understand the relation between halo mass and galaxy stellar mass is whether there is a third parameter that affects the mapping between these two masses. There is some evidence that this is indeed the case, as the relation between halo and stellar mass has a dependence on color that is fairly strong (e.g., Hearin et al. 2013; Rodríguez-Puebla et al. 2015). In fact, there are various ways in which the relation between the halo mass and stellar mass can be improved by investigating the detailed dependence on color as a proxy for star formation history and then explicitly accounting for it (e.g., Hearin et al. 2013, 2015; Rodríguez-Puebla et al. 2015).

Color is the easiest parameter beyond luminosity to measure for a galaxy, yet color itself depends on several factors, the most important of which is the timescale in which the galaxy is quenched. The fact that a galaxy's color is part of the extra parameterization of matching galaxies to halos can be seen in galactic conformity, whereby central and satellite galaxies within a halo have similar colors (i.e., both are either red or blue; e.g., Kauffmann et al. 2013). This relation holds even up to higher redshifts (Hartley et al. 2015), and therefore it is likely a fundamental way in which galaxy halo and stellar mass

Table 4
The Fitted Values of a, b, and c for the Relation between Stellar Mass, Halo
Mass, and $M_{\rm halo,vir}$ as Found through the Galacticus Simulation

Redshift	$\log M_* < 9.9$			$\log M_* > 9.9$		
	a	b	c	a	b	c
0.4	0.12	0.58	4.46	2.09	−0.82	−1.57
0.7	0.12	0.56	4.60	2.01	−0.68	−2.02
1.0	0.15	0.51	4.82	1.79	−0.40	−2.52
1.3	0.18	0.47	4.98	1.63	−0.24	−2.51
1.6	0.21	0.43	5.10	1.49	−0.06	−2.88
1.9	0.22	0.41	5.12	1.36	0.10	−3.15

Note. These values are used in Equation (7).

Table 5
The Fitted Values of a, b, and c for the Relation between Stellar Mass, Halo
Mass, and $C_{\rm vir}$ as Found through the Galacticus Simulation

Redshift	$\log M_* < 9.9$			$\log M_* > 9.9$		
	a	b	c	a	b	c
0.4	0.53	0.04	5.78	1.25	−0.05	−0.68
0.7	0.52	0.04	5.82	1.37	−0.02	−2.08
1.0	0.52	0.05	5.82	1.47	0.02	−3.46
1.3	0.51	0.07	5.82	1.49	0.06	−3.89
1.6	0.51	0.10	5.72	1.51	0.12	−4.35
1.9	0.50	0.16	5.53	1.52	0.16	−4.55

Note. These values are used in Equation (8).

relate. However, color is likely only an effect of a more fundamental underlying third parameter between the halo and stellar masses of galaxies, and we investigate this problem more broadly using our simulation results.

We investigate this third parameter effect using the Galacticus simulation output. In detail, we investigate how the scatter in the stellar mass–to–halo mass relation changes when considering other parameters.

Namely, we consider the merger history, the concentration of the virialized halo ($C_{\rm vir}$), the time when half of the mass of the halo was formed in Gyr since the Big Bang ($t_{\rm form}$), a combination of internal velocities of the halo $V_{\rm halo,max}$ and size at R_{200} ($R_{\rm halo}$) to measure a virial mass, and the dynamical mass as defined in Section 3.2. We convert the rotation and size into a virialized halo mass defined by

$$M_{\rm halo,vir} = \frac{V_{\rm halo}^2 \times R_{\rm halo}}{G}, \tag{6}$$

which is related to the dynamical mass but is a simpler formulation. Overall, what we find is that all of these values can act as a third parameter when investigating the relation between the stellar and halo mass.

To investigate this quantitatively, we consider a linear parameterization such that

$$\log M_{\rm halo} = a \times \log M_* + b \times M_{\rm halo,vir} + c, \tag{7}$$

$$\log M_{\rm halo} = a \times \log M_* + b \times C_{\rm vir} + c, \tag{8}$$

$$\log M_{\rm halo} = a \times \log M_* + b \times t_{\rm form} + c, \tag{9}$$

$$\log M_{\rm halo} = a \times \log M_* + b \times M_{\rm dyn} + c. \tag{10}$$

We show the resulting fitted values in Tables 4–7 for the best χ^2 fit using these three features as a third parameter. We find that at higher masses, the most effective third parameter for

Table 6
The Fitted Values of a, b, and c for the Relation between Stellar Mass, Halo Mass, and t_{Form} as Found through the Galacticus Simulation

Redshift	$\log M_* < 9.9$			$\log M_* > 9.9$		
	a	b	c	a	b	c
0.4	0.41	0.07	6.89	1.23	0.09	−1.31
0.7	0.41	0.09	6.89	1.29	0.11	−1.86
1.0	0.41	0.11	6.90	1.35	0.13	−2.40
1.3	0.41	0.14	6.94	1.33	0.16	−2.32
1.6	0.40	0.17	6.98	1.36	0.20	−2.59
1.9	0.39	0.21	7.03	1.38	0.24	−2.91

Note. These values are used in Equation (9).

Table 7
The Fitted Values of a, b, and c for the Relation between Stellar Mass, Halo Mass, and Dynamical Mass as Found through the Galacticus Simulation

Redshift	$\log M_* < 9.9$			$\log M_* > 9.9$		
	a	b	c	a	b	c
0.4	0.32	0.28	5.39	0.11	1.14	−0.97
0.7	0.36	0.25	5.31	0.13	1.22	−2.02
1.0	0.37	0.24	5.33	0.20	1.23	−2.86
1.3	0.38	0.23	5.38	0.33	1.13	−3.09
1.6	0.38	0.23	5.38	0.41	1.10	−3.51
1.9	0.38	0.23	5.36	0.50	1.00	−3.44

Note. These values are used in Equation (10).

reducing the scatter in the fit between the stellar and halo mass is the timescale in which the galaxy halo is assembled and the dynamical mass (Figure 3). Within the Galacticus simulation, this timescale is defined as the age of the universe when half of the halo mass is assembled. This correlates well, but with some scatter, with the time of the last major merger within this simulation.

We can also see from Figure 3 that there is a reduction in the scatter when considering the other possible third parameters, including the virial mass, dynamical mass, and halo concentration. These are all related, as the halo concentration correlates to the formation history of the halo, as well as to its color (e.g., Wechsler et al. 2002; Hearin & Watson 2013). This is not quite as simple in the Galacticus simulation, however, where the concentration for the main halos is determined by the halo mass, but it should be present for the satellite galaxies. This is because for satellites, the values of C and t_{form} will correlate, as the value of C is determined from when a satellite falls into a larger halo, and by definition, $t_{form} < t_{infall}$. However, for the bulk of the galaxies, this is not the case, which is one reason why concentration is not as good a third parameter as the other variables. Therefore, these four parameters appear to be the most suitable third parameters that allows us to use the relation between the stellar and halo mass to a higher accuracy.

If we take the example of the timescale of formation, as given by the t_{form} parameter, then the sense of this correlation is such that at a given stellar mass, the derived halo mass is higher if formation occurred at an earlier time. This implies that galaxies that formed earlier in the universe would have a higher value of M_*/M_{halo} than galaxies that formed later. We test this
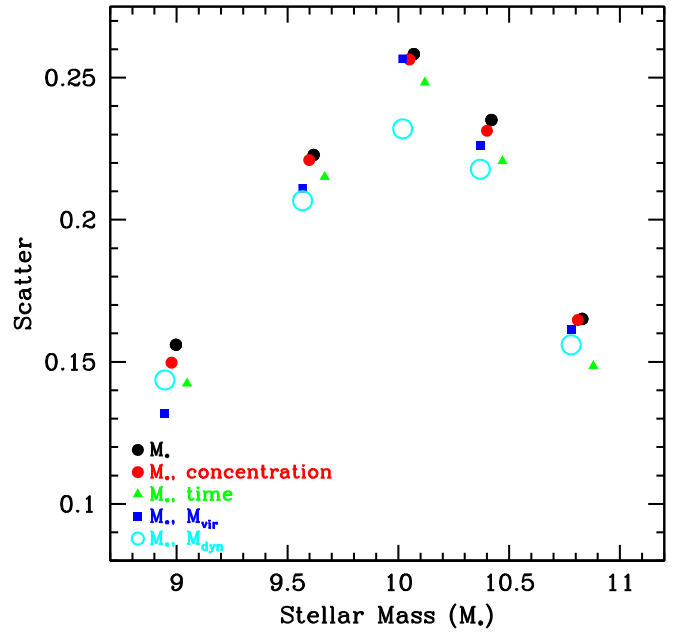

Figure 3. Scatter in the relation between the measured halo mass from the Galacticus simulation output and the predicted values based on various parameterizations using a third parameter (Section 4.2). The black points show the scatter when just considering the relation between the stellar mass of the galaxy and the halo mass. The red symbols show the relation when considering stellar mass and the halo concentration in a third parameter fit, while the green triangle shows this relation for the stellar mass and time of halo formation. Blue squares show the relation scatter when examining the fit between the stellar mass and virial mass, and the cyan circle is for the dynamical mass.

idea in Section 5.1. Note also from Figure 3 that the dynamical mass produces the lowest scatter between M_* and M_{halo}. This correlation is such that the dynamical mass is higher for higher-mass halos at a given fixed stellar mass.

To further demonstrate this, we show that the difference in the halo mass and the best-fit model mass based on just the stellar mass (Equation (5)) has residuals that correlate with both the dynamical mass and the timescale of formation (Figure 4). This is such that the scatter in the relationship correlates with each parameter, whereby those masses that are overfit (negative values) formed earlier and have lower dynamical masses, and those that are underfit (positive values) have later formation times and higher dynamical masses.

4.3. Halo Masses from Dynamical Masses Using Models

4.3.1. Methods and Results

Our goal in this section is to examine the relation between the observed dynamical mass and halo masses of galaxies at $z < 3$. We furthermore also investigate the use of the $S_{0.5}$ parameter for measuring the halo masses of galaxies.

One reason for investigating this in detail is that based on the results of Section 4.2, the scatter in the stellar mass–to–halo mass relation is reduced by including the dynamical masses, ages, and halo concentrations in the inference of halo mass from stellar mass. It might be the case, and indeed we later continue to show, that the relation between M_{dyn} and M_{halo} has a lower scatter and cleaner correlation than that between halo mass and stellar mass.

Based on this, we make the assumption that the dynamical mass is a better indicator of the halo mass than the stellar mass,
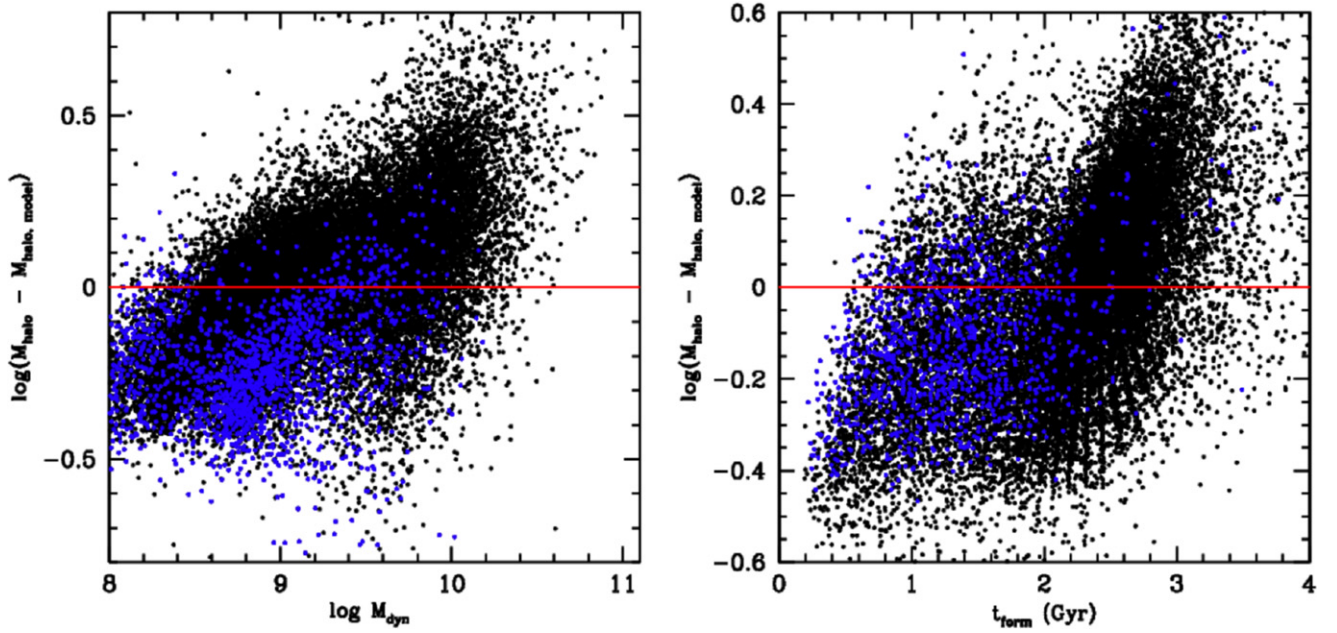
Figure 4. Relation between the halo mass of galaxies in the Galacticus simulation at $z = 1$ minus the model fit mass based on the stellar mass (Equation (5)). In the left panel, we show the correlation of this property with the dynamical mass, while in the right panel, we show it vs. the time of formation. The difference is such that systems that are overfitted by the average best fit have an earlier time of formation and a lower dynamical mass, whereas those systems that are more massive than the best fit formed later in the simulation and have a higher dynamical mass. The blue points in the left panel show systems that have a time of formation <1 Gyr, and on the right, the blue points are the systems that have a ratio of dynamical to halo mass <0.005.
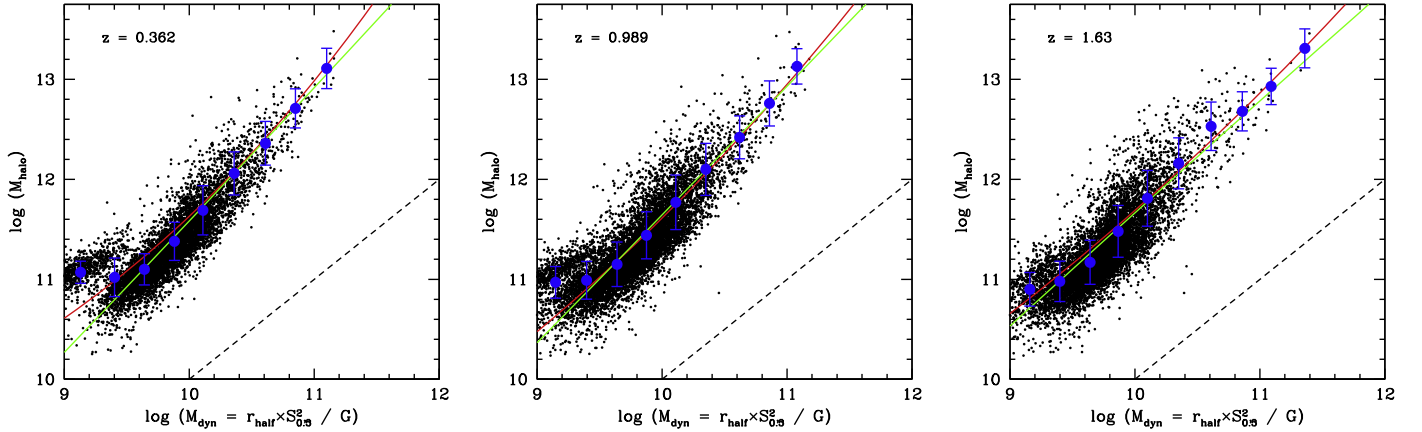
Figure 5. Relation between the dynamical mass, as measured with the $S_{0.5}$ parameter (Section 3.2), and the halo mass from the Galacticus simulation. The dashed line shows where the 1:1 ratio for these parameters would be, while the red line shows the best-fitting relationship between the halo and dynamical mass. The green line shows the Moster et al. (2010) fitting formalism to this relation (see Appendix).

as not only does it have a reduced scatter, but it is also a measure of the internal motions of galaxies, and thus more directly aligned with a measurement of the halo properties than the stellar mass, which is based on complicated baryonic physics and star formation histories (e.g., Hearin & Watson 2013).

We investigate this using both the Galacticus and Millennium simulation results. We find that the two models give essentially the same pattern between the dynamical mass and halo mass. We use the values of the half-mass radius, velocity dispersion, and maximum rotational velocity from the Galacticus simulation to determine the relation between $M_{\rm dyn}$ and $M_{\rm halo}$ using the calculation of $M_{\rm dyn}$ from Equation (2), as well as when we use the $V_{\rm max}$ value instead of $S_{0.5}$.

When we compare the relationship between $M_{\rm dyn}$, as measured using $S_{0.5}$, and the halo mass, we obtain Figure 5.

The best-fitting relation between these parameters is given by

$$\log(M_{\rm halo}) = \gamma \log(M_{\rm dyn}) + \delta. \quad (11)$$

We list the values for γ and δ in Table 8. As can be seen, there is very little evolution in redshift in these parameters, and in fact, on average, the predicted dynamical mass–to–total mass relation does not change much up to $z = 2$ in these models.

We now ask the question of whether it is better to use these dynamical masses or stellar masses to obtain $M_{\rm halo}$. Essentially, we want to derive $M_{\rm halo}$ from observations, and it is likely that M_* or some form of dynamical mass is the best way to do this. For a method of deriving $M_{\rm halo}$ to work well, we want a maximum sensitivity; i.e., as you move along the "observed" axis, small changes produce a significant amount of change in the halo mass measure. Flat relations like that seen for the σ mass in Section 4.3.3 have "shallow" fits where similar halo

Table 8
The Fitted Values of α and β for the Relation between Dynamical Mass and Halo Mass Using the Results of the Galacticus Simulation

Redshift	γ	δ
0.4	1.34 ± 0.02	-1.80 ± 0.26
0.7	1.21 ± 0.02	-0.43 ± 0.23
1.0	1.29 ± 0.04	-1.22 ± 0.40
1.3	1.21 ± 0.02	-0.43 ± 0.23
1.6	1.20 ± 0.03	-0.30 ± 0.26
1.9	1.21 ± 0.05	-0.45 ± 0.45

Note. These values are used in Equation (5) and are generally best used for systems with larger stellar masses, e.g., $\log M_* > 10$.

masses are retrieved for a range of "kinematic" masses. However, we also do not want a very steep relationship, such that small changes in observables produce large changes in halo masses. This is because all observables have uncertainties, and inaccuracies are magnified by a very steep relationship.

Ideally, we want something that has a 1:1 slope as much as possible, and this is provided more by the relation between dynamical and halo masses than by that between stellar and halo masses. This can be seen by the slopes in the $M_{\rm dyn}$ versus $M_{\rm halo}$ relations shown in Table 8 that have values of $\sim 1.2-1.3$. This way, galaxy halos can be derived with maximum sensitivity without inducing large errors. Note that these criteria for deriving maximum usability are in concert with minimizing the scatter, which $M_{\rm dyn}$ versus $M_{\rm halo}$ also does (Figure 3).

Therefore, we conclude that using a dynamical mass is superior to using a stellar mass to obtain the halo mass. Using the Moster et al. (2010) formalism (see Appendix), we are also able to retrieve a good fit, particularly for the lower-mass galaxies. We hereafter use this as the model method for finding the total halo masses of galaxies based on their dynamical masses as measured from the kinematics and sizes of galaxies.

However, it must be noted that in a real sense, these "measures" are model-dependent, and as such, when we compare with other methods of measuring the halo mass, we are in a sense testing this methodology for measuring the halo masses of galaxies based on observational features. This methodology is thus not ideal, as it relies on semi-analytical models and is not based on fundamental observations or derivations. However, if the mass profile of real galaxies is similar to those in the models we use, our methodology should be effective at tracing the halo masses of individual galaxies. Importantly, this method is superior to just using the stellar mass.

This is also not fundamentally different from halo masses measured through abundance matching or clustering, where there is an assumption about dark matter halo masses and how these are distributed in abundances and clustering. Alternative methods of deriving and their comparisons between the total masses from lensing or the kinematics of large radii tracers such as clustering will be addressed below.

4.3.2. Comparison to Virial Mass at Virial Radius

Another direct way to measure the total or halo mass of a galaxy is to use, for disk-like galaxies, the circular velocities and virial radius to make a measurement of the halo mass. This can be done using theoretical arguments that relate observed quantities of the effective radius to the virial radius, as well as

the circular velocity to the $V_{\rm max}$ values that are measured directly from the data.

This can be done in the following way, as first outlined in a similar way in Lampichler et al. (2017). The relationship between the effective radius and the virial radius is given by Kravtsov (2013) and Agertz & Kravtsov (2016) using the abundance-matching assumption that $n_{\rm h}(>M) = n_g(>M_*)$, such that

$$R_{200} = 66.67 r_{1/2}.$$

This equation, however, requires us to know the half-mass radius, as opposed to the half-light or effective radius, which is what we have measured for the bulk of our galaxies. However, when the half-light radius is compared to the half-mass radius using the mass maps of galaxies, there is little systematic difference found. Therefore, we use the value of the effective radius when measuring the virial mass through this method, i.e., $r_{1/2} = r_{\rm eff}$ (e.g., Lanyon-Foster et al. 2012).

The next step when converting observations to virial masses through this method requires that we use the circular velocity rather than the maximum velocity. For this, we find that the circular velocity–to–maximum velocity ratio is given by Cattaneo et al. (2014) such that $v_{\rm circ} = 1.33 \times V_{\rm max}$. We compare our masses measured through this approach using the equation

$$M_{\rm circ} = \frac{V_{\rm circ}^2 \times R_{1/2}}{G} = \frac{1.33 \times V_{\rm max}^2 \times R_{1/2}}{G}, \qquad (12)$$

which we call the circular masses. We compare these masses with those obtained through our direct approach. The result is shown at three different redshifts in Figure 6, where there is a good overlap with the mass measurements using our approach. This is particularly the case for those systems that are rotationally dominated with $v/\sigma > 1$, as shown by the blue points in Figure 6. The analytical relation goes through these points except at the highest masses.

4.3.3. σ Masses—Early-Type Galaxies

A popular method for obtaining the total masses of early-type galaxies or ellipticals that are dominated by their velocity dispersion is to use the formula

$$M_{\rm sig} = \frac{5 \times \sigma^2 \times R_e}{G}, \qquad (13)$$

which we call the σ mass. This is often used to determine the total masses of galaxies, even at high redshifts (e.g., Treu et al. 2005). We show in Figure 7 the relationship between the σ mass and the halo mass found within the Galacticus models. We find that the σ mass is a good tracer of the halo mass at the highest masses, where $\log M_{\rm sig} > 12.5$, but note that the highest-mass end of this relation is dominated by galaxies with large sizes.

We also plot this ratio between the halo mass and σ mass in the right panel of Figure 7. This demonstrates that the halo mass of the highest-mass elliptical galaxies can be retrieved from the measurement of internal velocity dispersions (σ) for most but not all of these high-σ galaxies.

We furthermore find that the relation between the halo mass and σ mass is not well fit by a power law between the two, as we find for the halo mass and dynamical $S_{0.5}$ mass. In fact, we
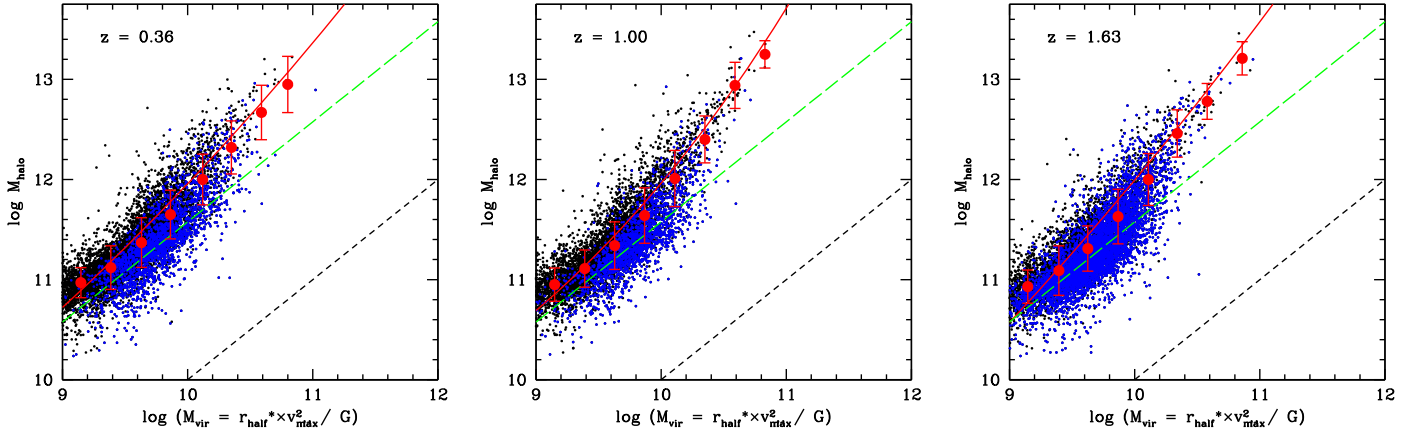
Figure 6. Relation between the circular velocity mass (Section 4.3.2) as measured with the V_{max} parameter and the halo mass from the Galacticus simulation. This is a typical method for finding the masses of disk-like or rotating galaxies. The blue points show the rotation-dominated systems that have a $V_{max}/\sigma > 1$. The black dashed line shows where the 1:1 ratio for these parameters would be, while the red solid line shows the best-fitting relationship between the halo and virial masses. The green long-dashed line shows the value of the halo mass derived from the circular mass when using the analytical relation of half-light radius to virial radius (Equation (12)).

find a good fit when we use the formalism between halo and stellar mass found by Moster et al. (2010) derived from abundance-match samples. We show this best fit as the red line in Figure 7. We discuss this relation in more detail in the Appendix.

4.4. Abundance-matching Masses

We further investigate the halo mass–to–stellar mass ratios from halo abundance matching using stellar masses calculated using the same methodology and underlying techniques as we do for the primary sample's stellar masses. The basic idea behind this method is to use measured stellar mass number densities at various redshifts and dark matter relation predictions to determine the halo masses for systems with the same abundances (e.g., Kravtsov et al. 2004; Shankar et al. 2006; Conroy et al. 2007; Behroozi et al. 2013; Moster et al. 2013; Shankar et al. 2014; Buchan & Shankar 2016).

Our primary method is to use the number densities for galaxies as a function of redshift as derived by Mortlock et al. (2015), who furthermore use the Chabrier IMF and fitting methods that we use for our measured stellar masses when comparing with kinematic dynamical masses. We then match these number densities, which get higher at lower masses, to those of dark matter halo abundances at the same redshifts and thereby associate each mass range with a halo mass range.

To carry out this comparison, the mass function of dark matter halos (including subhalos) is assumed to be monotonically related to the observed stellar mass function of galaxies with zero scatter. This relation is given by

$$n_g(>M_{star}) = n_h(>M_{halo}), \qquad (14)$$

where n_g and n_h are the number densities of galaxies and dark matter halos, respectively.

To derive these, we use the Jenkins et al. (2001) modification to the Sheth & Tormen (1999) halo mass function and the analytic halo model of Seljak (2000) and generate the linear power spectrum using the fitting formulae of Eisenstein & Hu (1998). Based on this, the predicted number density of dark matter halos is given by

$$n_h(>M_{halo}) = \bar{\rho} \int_{M_{min}}^{\inf} \frac{\langle N \rangle}{M_{halo}} f(\nu) d\nu, \qquad (15)$$

where $f(\nu)$ is the scale-independent halo mass function, $\nu = [\delta_c/\sigma(M_{halo})]^2$ ($\delta_c = 1.68$ is the value for spherical overdensity collapse), $\sigma(M_{halo})^2$ is the variance in spheres of matter in the linear power spectrum, $\bar{\rho}$ is the mean density of the universe, and $\langle N \rangle$ is the average number of halos, including subhalos, where we assume the fraction of subhalos (f_{sub}) is described by

$$f_{sub} = 0.2 - \frac{0.1}{3} z, \qquad (16)$$

as in Conroy & Wechsler (2009). Note that this fraction is small and therefore has little effect on our results, but we include it for completeness. Our method basically assigns the most massive galaxies, as measured in stellar mass, to the most massive halos. Given its simplicity, it is reasonably successful at matching various observations at multiple epochs (e.g., mass-to-light ratios and clustering measurements; see Conroy & Wechsler 2009 and references therein).

We find that the fits between the stellar mass and halo mass with abundance matching is well represented by the following analytical functions at $z = 0.40, 0.75, 1.25, 1.75, 2.25$, and 2.75 as

$$\log M_{halo} = a(\log M_*)^b + c, \qquad (17)$$

which are all fit with low χ^2 values. The results of these fits are shown in Table 9. This differs slightly from other parameterizations that include up to five parameters (Behroozi et al. 2013), yet this is the simplest form that fits our data.

We compare the relation between the halo masses derived from abundance matching and the stellar masses at the same limits in Figure 8. The halo masses derived from abundance matching are derived based on the most massive galaxies at each corresponding stellar mass. Thus, it is possible, even likely, that galaxies that are within larger halos are found to have higher halo masses at a lower stellar mass through abundance matching than what we find through the model masses derived in Section 4.1.

We show this comparison at redshifts from $z = 0.4$ to 3. First, we note that there is a small amount of evolution in the halo to stellar mass ratio as a function of redshift, which is also what we find when we investigate this relationship using the
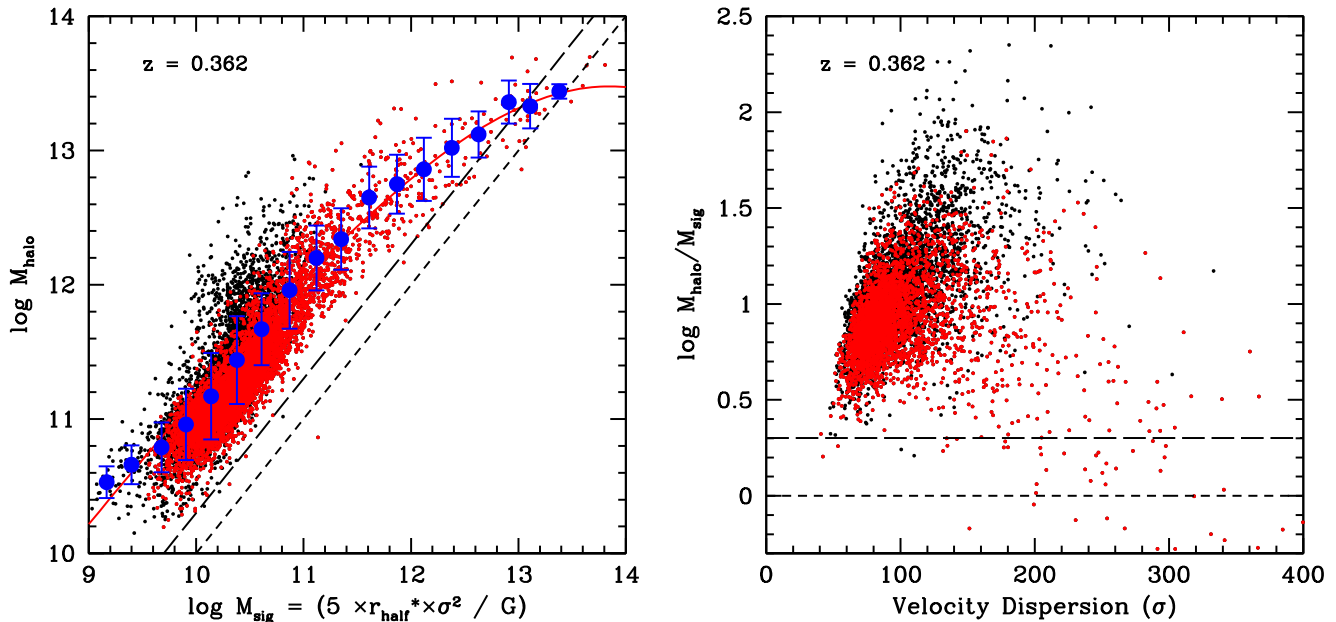
Figure 7. Figures showing the singular use of the velocity dispersion to retrieve the halo masses of galaxies. The left panel shows the relation between the σ mass (see text) and halo mass from the Galacticus models. The blue points show the averages of all galaxies, while the red points show galaxies with a ratio of rotational velocity and velocity dispersion such that $(V_{max}/\sigma) < 1$. The solid red line shows the best fit between the σ mass and halo mass using the formalism from Moster et al. (2010). The short-dashed lines show the 1:1 ratio, while the long-dashed lines show the ratio of 2:1 for underestimating the halo mass by a factor of two based on the σ mass. The right panel shows the difference between the halo mass and σ mass for galaxies at $z = 0.362$. The two horizontal lines show the 1:1 and 2:1 ratio as described for the left panel.

Table 9
The Fitted Values for Equation (17) that Relate the Stellar Mass and Halo Mass for Galaxies Using Abundance Matching (Section 4.4)

Redshift	a ($\times 10^{-10}$)	b	c
0.40	3.68 ± 0.25	9.27 ± 0.28	11.22
0.70	2.68 ± 0.29	9.41 ± 0.28	11.22
1.25	2.73 ± 0.38	8.53 ± 0.16	11.22
1.75	8.28 ± 0.35	8.00 ± 0.05	11.22
2.25	2.69 ± 0.34	8.46 ± 0.05	11.22
2.75	3.64 ± 0.77	6.39 ± 0.08	11.22

observable relations from the simulation output (Section 4.1). However, we note that at $z > 1.5$, the relation is higher, such that the halo mass is larger at a given stellar mass, particularly at lower masses. At higher masses, the trend is not as clear.

We also overplot in Figure 8 the relation between halo and stellar mass derived from the model masses derived from stellar mass (Equation (5), Section 4.1) at redshifts $z \sim 0.4$ and 1.0. There are some differences between the abundance-matched–based masses and the stellar mass–based model masses, particularly at the lower-mass range; however, this is due to the fact that there is unlikely to be a 1:1 galaxy:halo ratio at these masses, something we investigate and discuss further below. Hence, we get an overestimate of the individual halo masses for these systems using abundance matching. This is not an unexpected result to some degree within this formalism, and this effect has been seen before by, e.g., Conroy & Wechsler (2009). We compare the calculated halo masses as a function of stellar mass using the model approach from Equation (5) to those from abundance matching in Figure 9, which shows the ratio of the halo model masses versus the abundance-matching masses.

Overall, we find that the average difference between the two methods of measuring M_{halo} is less than a factor of three at log

$M_* > 10.5$, which is the primary mass range we study here. This difference is such that the abundance-matching masses overestimate the halo masses by a factor of roughly 1.5–3 compared to dynamically based halo masses at log $M_* < 11$. The halo masses are similar within these two methods at the highest masses. However, at log $M_* < 10$, the difference is large, a factor of ~ 4, between the abundance-matching–based masses and those from the models. This is likely due to abundance matching locating these lower-mass galaxies in overall higher halos as few systems are isolated.

This shows that our method of measuring the halo masses for massive galaxies through models is roughly consistent with other independent methods at the highest masses and thus likely to be reliable given that halo abundance matching reveals nearly the same halo masses for a given stellar mass in the range we are interested in, with an uncertainty similar to that of measuring the stellar masses. We furthermore compare our results to other abundance-matching results, as well as with gravitational-lensing ones in Section 5.

5. Observational Results

In this observational results section, we first describe the relations between the various masses calculated in Sections 3 and 4 for actual galaxies, including using our new derived individual halo masses. This is followed by a discussion of how these results can be applied toward understanding how galaxy assembly occurs in terms of its major mass components. Later, in the discussion section, we discuss the implications of these results.

5.1. Mass-scaling Relations

In this section, we use the various measured and calculated stellar, dynamic, and halo masses to link the stellar and dark masses of galaxies up to $z \sim 1.2$ for our mostly star-forming
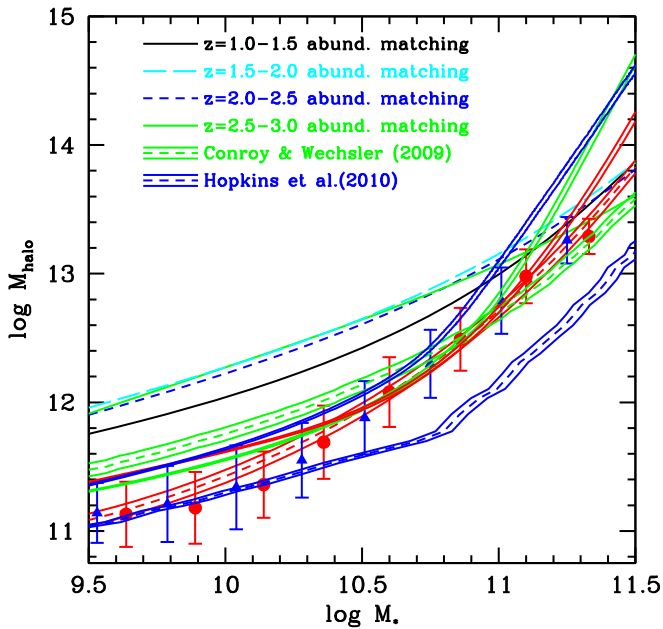
Figure 8. Relation between stellar mass and halo mass as derived through abundance matching and weak lensing. Shown are four lines from this method representing the relationship between these two quantities from $z = 1$ to 3, as shown by the curved single lines. The points (red for $z \sim 1$ and blue for $z \sim 0.4$) show the relationship between the stellar and halo masses as derived through the Galacticus simulation (Section 4.1). The dashed red line surrounded by two solid lines shows the best-fitting relationship for this simulation at $z \sim 1$. The double solid green line is the relationship between stellar and halo mass from weak-lensing measures from van Uitert et al. (2016), the double solid red line is from the lensing results of Leauthaud et al. (2012), and the double blue solid line is from Moster et al. (2013). We also show the abundance-matching stellar and halo masses from Hopkins et al. (2010) and Conroy & Wechsler (2009).

Figure 9. Plot showing the ratio between the halo masses measured with abundance matching (and weak lensing) at a given stellar mass from $\log_* = 9.5$ to 11.5 compared to the predictions from the Galacticus simulation (Section 4.1). The key shows similar lines as in Figure 8. The double solid green line is the relationship between stellar and halo mass from weak-lensing measurements from van Uitert et al. (2016), the double solid red line is from the lensing results of Leauthaud et al. (2012), and the double blue solid line is from Moster et al. (2013). As in Figure 8, the blue dashed line surrounded by two solid lines is from Hopkins et al. (2010), and the green dashed line surrounded by two solid lines is from Conroy & Wechsler (2009). The horizontal line shows where our measurement of halo mass from Galacticus is identical to these other methods.

primary sample. This includes investigating how stellar mass relates to these other masses observationally. Ultimately, we are interested in applying these relations to data to infer galaxy evolution, which we discuss in Section 6.

5.1.1. The Tully–Fisher Relation

For a first step toward investigating the evolution of the different dark masses in galaxies, we construct a TFR for our sample and compare this to the simulation data that we use to convert dynamical into halo masses. Using the primary sample in this paper, Kassin et al. (2007) used the $S_{0.5}$ parameter to construct a new type of stellar mass TFR that takes into account the ionized gas velocity dispersion ($S_{0.5}/M_*$ TFR; hereafter kinematic TFR). The form of this TFR is given by

$$M_* = a \times \log S_{0.5} + b,$$

where a is the slope of the relation and b is the intercept. This kinematic TFR is considerably tighter than TFRs calculated without taking into account the velocity dispersion and has no detectable evolution over the redshift range $0.1 < z < 1$.

We show the $S_{0.5}$ TFR in Figure 10 at redshifts $z < 1.2$ and $z > 1.2$. As can be seen, there is a good relationship between the stellar mass and the values of $S_{0.5}$ at both high and low redshifts. This involves galaxies of different types. Furthermore, we also plot in these relations the prediction between these two quantities at both high and low redshift from the Galacticus simulation output. As can furthermore be seen, we find a good agreement with the location of our data and
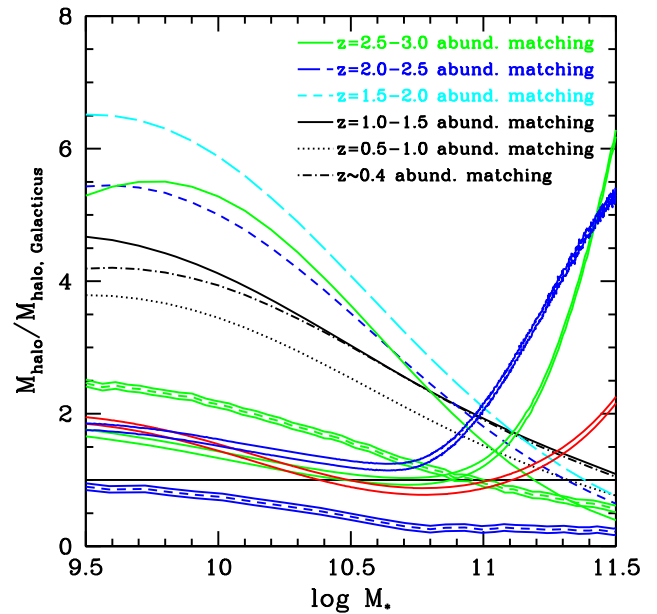
theoretical model output, demonstrating that we can use these simulations as a good cosmological representation of all galaxies up to $z \sim 3$.

5.1.2. Dynamical and Stellar Masses

In this section, we compare the dynamical masses in our primary sample from Equation (2) to their corresponding stellar mass measurements. We plot the dynamical masses for the primary sample as a function of stellar mass in Figure 11. We fit the stellar-to-dynamical mass relation for this primary sample as

$$\log (M_{\rm dyn}) = (0.71 \pm 0.02)\log (M_*) + (3.17 \pm 0.17). \quad (18)$$

From Figure 11, it is clear that the dynamical mass, as we define it, within the visible radius is dominated by the baryonic and stellar mass. As can also be seen in Figure 11, it is clear that this ratio of dynamical to stellar mass does not change significantly at different redshifts up to $z \sim 3$.

There is an interesting feature in the stellar-to-dynamical mass plot that deserves a more careful look. This is the fact that the stellar mass for the primary sample, as well as the elliptical sample from Treu et al. (2005), has the interesting property that the stellar mass is higher than the dynamical mass. This is certainly partially due to the way in which we define the dynamical mass and how it gives a better idea of the total mass for elongated and rotating systems than for compact systems such as ellipticals. The reason for this has to do with the fact that the total mass of spheroids is usually calculated with a constant in front of our dynamical mass equation, with most
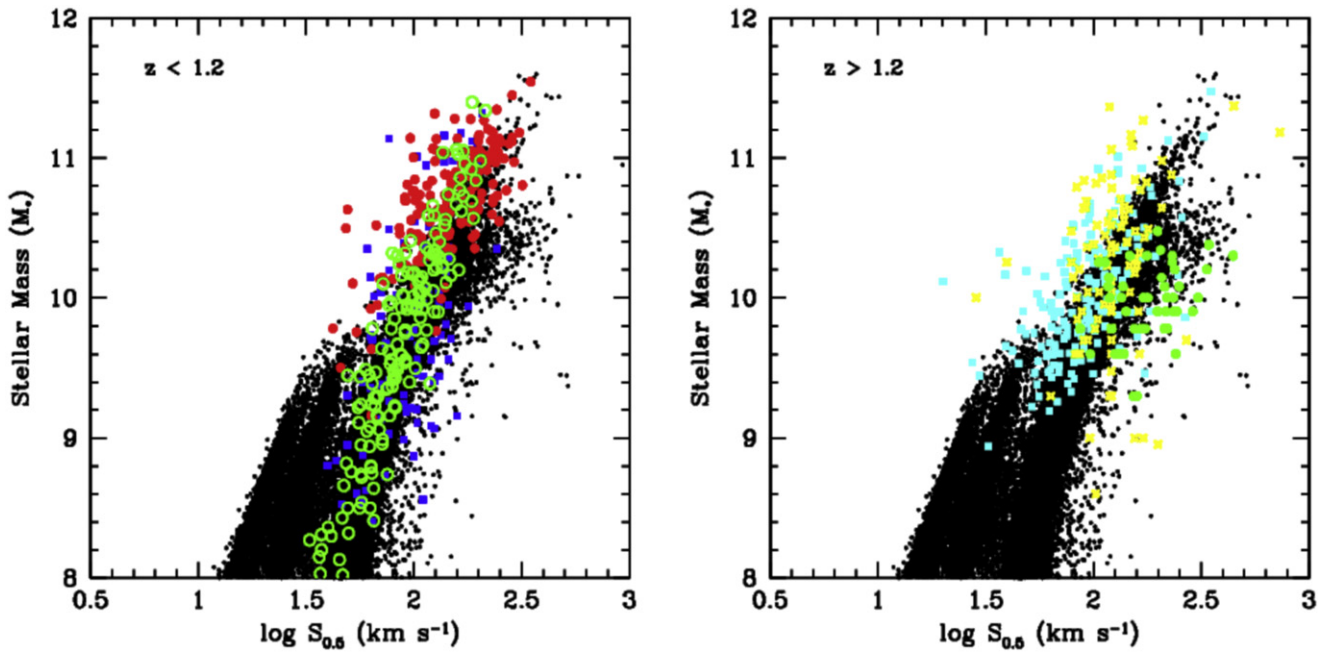
Figure 10. $S_{0.5}$ stellar mass TFR for our sample of galaxies, as well as for the Galacticus models we use to calculate the halo masses from dynamical masses. Shown on the left are the values for the $z < 1.2$ galaxies, while the right panel shows the values for galaxies at $z > 1.2$. In the left panel, the blue squares are for the disk galaxies from Conselice et al. (2005), the green circles are for the disk galaxies in Miller et al. (2011, 2014), and the red circles are for the ellipticals at $z < 1.2$ taken from Treu et al. (2005). For the higher redshifts on the right, the cyan squares are for the MOSDEF data from Price et al. (2016), the yellow crosses are for Erb et al. (2006), and the green circles are for Förster Schreiber et al. (2006).

using "5" (see Section 4.3.3). This is 0.7 dex, which is roughly the amount of the difference seen between the 1:1 ratio and the location of where ellipticals are located, both in the Treu et al. sample and our primary sample.

We furthermore use these relations to derive how the ratio of the stellar mass to dynamical mass changes with both dynamical and stellar mass. We find overall that these relations are indeed quantitatively relatively constant as a function of redshift. Examining the relationship between stellar and dynamical mass, we find a best fit of

$$\log\left(\frac{M_*}{M_{\rm dyn}}\right) = 0.41 \times \log M_{\rm dyn} - 4.64, \qquad (19)$$

and for the relation in terms of stellar mass, we find

$$\log\left(\frac{M_*}{M_{\rm dyn}}\right) = 0.29 \times \log M_* - 3.17. \qquad (20)$$

Overall, this reveals that the stellar mass ratio goes as $M_*/M_{\rm dyn} \sim M_{\rm dyn}^{0.41}$ and $M_*/M_{\rm dyn} \sim M_*^{0.29}$. This shows that within the visible extent of galaxies, the efficiency of galaxy assembly, defined as having higher M_* to total mass, is larger at higher dynamical and stellar masses up to our limit of log $M_* \sim 11$ (Figure 1).

We plot the ratio of stellar mass to dynamical β mass against redshift in Figure 12 for our primary sample divided into morphological types and in Figure 13 for the total sample. We find that the evolution of this ratio with redshift over the entire sample can be fit as

$$\left(\frac{M_*}{M_{\rm dyn}}\right) = (1.49 \pm 0.17)(1 + z)^{0.30 \pm 0.12}. \qquad (21)$$

However, the bulk of this evolution occurs at $z < 1$. If we carry out this fit at $1 < z < 3$, we find a flat slope with $(M_*/M_{\rm dyn}) \sim (1 + z)^{0.18 \pm 0.41}$. On the other hand, we find an increase from $z \sim 0$ to 1 such that $(M_*/M_{\rm dyn}) = 1.37 \pm 0.60 \times (1 + z)^{0.86 + 0.47}$.

This essentially means that there is very little to no evolution in the ratio of stellar to dynamical masses at the highest redshifts. A caveat must be given, however, as our samples at higher redshifts are probably not representative. However, we are likely sampling the more gas-rich galaxies at these redshifts. Thus, we would expect that value to increase, yet it remains statically flat, at least in our overall sample.

As a further way to test this, we investigate the BOSS sample from SDSS-III using galaxies with high masses at $M_* > 10^{11} M_\odot$, typically higher than those considered in this paper. In Figure 14, we show this relationship for galaxies from the BOSS sample at $z < 0.7$. When we do a least-squares fit to this relationship between stellar-to-σ mass ratio for galaxies in the range $M_* = 10^{11} - 10^{11.5} M_\odot$ and redshift, we find the relationship

$$\left(\frac{M_*}{M_{\rm dyn}}\right) = (0.30 \pm 0.01)(1 + z)^{1.85 \pm 0.1}, \qquad (22)$$

where there is a slight increase with redshift in this ratio for the entire BOSS sample. This implies as well that there is some evidence for evolution in this ratio at $z < 1$ within the highest-mass galaxies. We investigate this relationship for higher-redshift systems in Section 5.2 using the total halo masses of our systems.

Furthermore, Figure 12 is also plotted by morphological type as measured by the CAS parameters (Section 2.2). Based on this, we find that the early-type systems have a slightly higher stellar-to-dynamical mass ratio than other morphological types
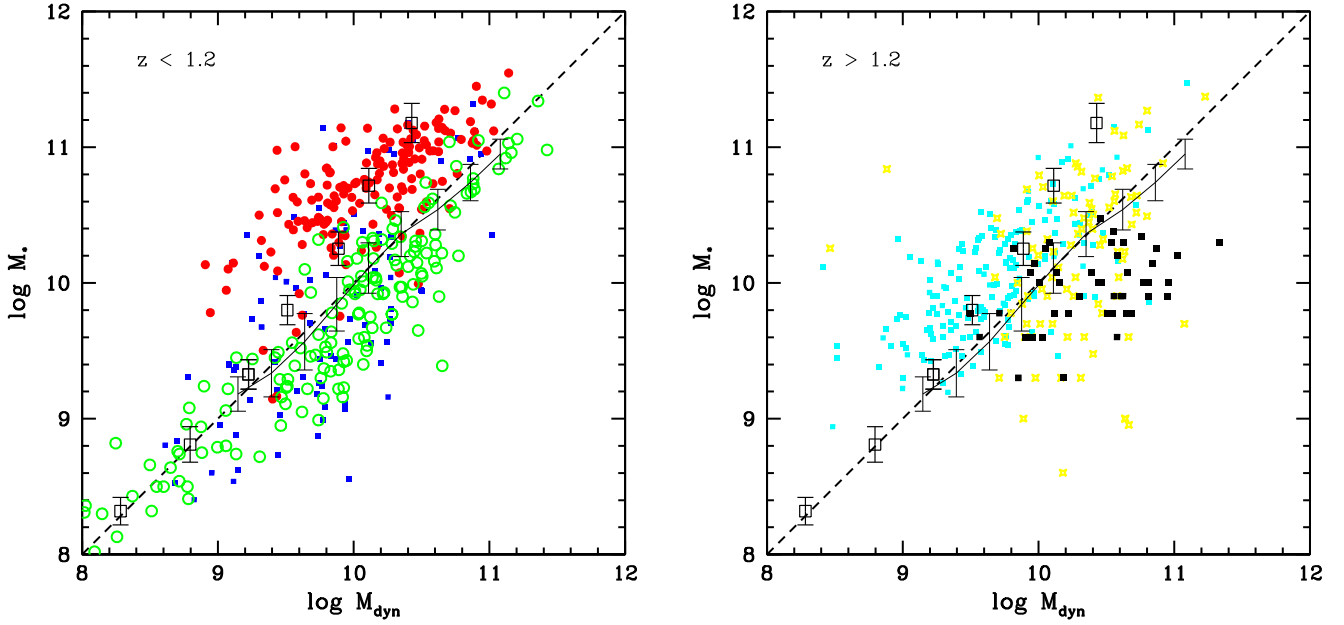
Figure 11. Figure showing the relationship between the stellar and dynamical mass divided into two redshift bins, with the left panel for galaxies at $z < 1.2$ and the right panel for $z > 1.2$ systems. The open squares with error bars show the average and scatter of the primary sample. The blue filled squares are for the disk galaxies from Conselice et al. (2005), the green circles are for the disk galaxies in Miller et al. (2011, 2014), and the red circles are for the ellipticals at $z < 1.2$ taken from Treu et al. (2005). For the higher redshifts on the right, the cyan squares are for the MOSDEF data from Price et al. (2016), the yellow crosses are for Erb et al. (2006), and the black filled squares are for Förster Schreiber et al. (2006). A key to this is shown in Figure 13. The solid line with error bars shows the model relationship between these two quantities as derived in the Galacticus models (see Appendix A).
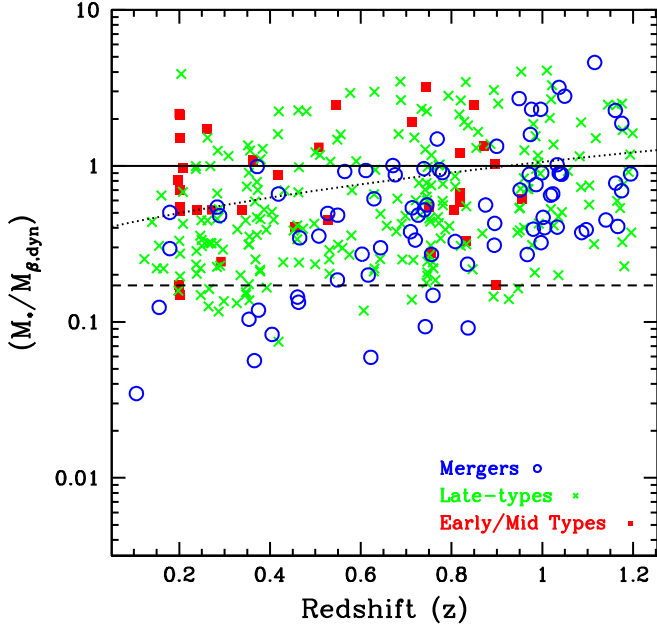
Figure 12. Stellar-to-dynamical β mass (Equation (3)) ratio with respect to redshift for the primary sample. The points are colored by the CAS morphological type. There is some evidence for a change in the ratio with redshift, although we do see a stronger trend in the differences between morphological types, such that mergers and disks have a lower stellar mass–to–dynamical mass ratio than early-type galaxies. The straight dot-dash line is the universal baryonic ratio, and the dotted line is the best fit to the data.

Figure 13. Relationship between the ratio of dynamical to stellar mass as a function of redshift. The colors of the points are the same as in Figure 11. The long-dashed line shows the best fit to this relationship from low redshift to the highest redshifts at $z \sim 3$. The short-dashed line shows the relationship between this mass ratio and redshift fitted up to $z \sim 1.3$. We find little significant evolution at $z > 1$ in this relationship with the relation through all redshifts going as $\sim (1 + z)^{0.3 \pm 0.12}$ (see the text).

at all redshifts. This is potentially a sign that the efficiency of galaxy formation is higher in early-type galaxies than in disks/late types/mergers. This is not a trend that results from the early-type galaxies being more massive; as in our primary sample, the ellipticals are not more massive on average than the other morphological types (Figure 1). This shows
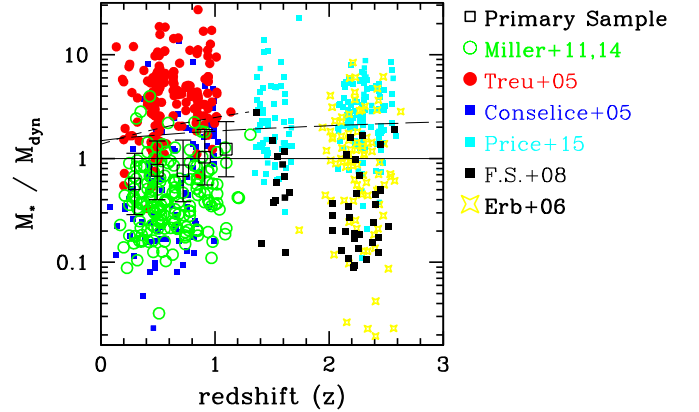
observationally that there is a third parameter in the relation of dynamical mass to halo mass, consistent with age as a third parameter, as discussed in Section 4.2. This must be related to the galaxy morphology and time of formation that correlates with the concentration of the halo/galaxy. We investigate this in more detail in Section 6.

5.1.3. Halo Mass versus Stellar Masses

We now use these results to examine the relation between the halo and the stellar mass for our sample of real galaxies. We show in Figure 15 the halo masses derived from Section 4 as a function of stellar mass for our entire observational sample. The dashed black line shows the best three-component theory
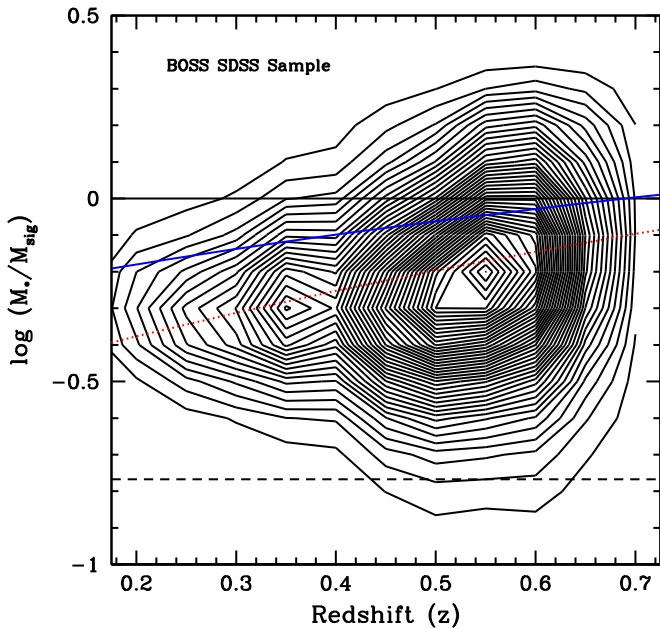
Figure 14. Relationship between the σ masses and stellar masses for the 180,000 galaxies in the BOSS sample as part of the SDSS sample in DR7 (Beifiori et al. 2014). The red dotted line shows the best fit for the data, while the blue solid line shows the best fit for the relation for our total sample but using the dynamical mass instead of the σ mass.

fit from Equation (5), showing a reasonably good agreement with the data at the highest masses. We attempt to improve the above fit and minimize scatter by investigating the stellar-to-halo mass fit when galaxies are binned by morphology and stellar mass density. There is a slight improvement in these fits when the sample is binned by morphological type or stellar mass surface density.

Figure 16 shows the stellar mass–to–halo mass ratio as a function of stellar mass for our entire sample using both primary and secondary sources. To compare our halo masses with those of other work, we plot our results with those of Foucaud et al. (2010), van Uitert et al. (2016), Leauthaud et al. (2012), and Moster et al. (2013). These studies use different techniques to measure the halo masses of galaxies as described in Section 2.4. The observational studies are shown as points of various shapes and colors.

In the mass range $10^{10.5} < M_*/M_\odot < 10^{12.0}$, we broadly agree with previous results, except for the Treu et al. (2005) ellipticals. There is also an interesting feature in these figures such that there is no obvious turnover in the M_*/M_{halo} ratio, which reaches a maximum at about log $M_{halo} = 11.5$. This turnover is seen in other samples at this halo mass based on clustering (e.g., Foucaud et al. 2010; Coupon et al. 2012). For example, the peak found by Coupon et al. (2012) is log $M_{halo} = 11.6$ from clustering, and in Coupon et al. (2015), it is log $M_{halo} = 12.2$. We are able to probe down to log $M_{halo} = 13$, yet we do not see an obvious turnover in the ratio of stellar to halo mass to this limit.

This shows that the efficiency of galaxy formation is highest at the highest masses. This relationship is also seen when one compares the mass ratios by using halo masses as determined from abundance matching (e.g., Behroozi et al. 2013). Figure 17 furthermore shows the ratio of our abundance-matching stellar versus halo masses as a function of stellar mass. This demonstrates that the maximum galaxy formation

efficiency is at around log $M_* \sim 10.5$. Finally, Figure 18 shows the evolution of the ratio of stellar to halo mass as a function of redshift, demonstrating little change with time, as discussed in the following section.

5.2. Mass Ratios as a Function of Redshift

One of the issues we investigate is how the ratio of stellar to halo mass varies with redshift. This is, however, a difficult topic to study observationally, and our attempts at answering this question should be seen as a preliminary solution until more kinematic and mass data are available for complete samples of galaxies at $z > 1.5$. However, we can get some idea of this from limited observations of kinematics at various redshifts, as well as through our abundance-matched masses.

Overall, however, as we have kinematic data up to $z = 3$, we can determine the evolution of this relation up to these redshifts, although for a potentially biased sample of mostly star-forming galaxies (Section 2.3). Figures 12 and 13 plot stellar-to-dynamical mass ratios as a function of redshift up to $z = 1.2$ for our primary and total sample, while Figure 19 plots the M_*/M_{halo} ratio against redshift for all of the observational samples compared with theory predictions and other observational results. For all samples of galaxies up to $z = 3$, we find a best-fitting relationship of the form

$$f_{*,halo} = \left(\frac{M_*}{M_{halo}}\right) = (0.07 \pm 0.01) \times (1 + z)^{-0.07 \pm 0.11}. \quad (23)$$

This is consistent, within 1σ, of this ratio being flat; i.e., it does not evolve with redshift. We do find an evolution with a significant slope for the sample at $z < 1$ with $f_{*,halo} = 0.028(1 + z)^{1.97 \pm 0.29}$, as we do for the ratio of the dynamical to stellar mass.

This shows that the majority of the evolution in terms of stellar versus halo mass occurs at later times when galaxies are primarily finished with their star formation and are evolving more in terms of galaxy mergers (e.g., Mundy et al. 2017). In summary, we find no significant evidence for any change in the M_*/M_{dyn} ratio at the highest redshift, although we do find an evolving ratio at lower redshifts, $z < 1$.

We also find very little evolution in the stellar-to-halo mass ratio when using the abundance-matching technique (Section 4.4). We show in Figure 18 the evolution of the ratio of stellar to halo mass as derived from the abundance-matching methodology. Overall, we find that the stellar mass ratio does not significantly evolve with time at any measured stellar mass as measured either from the kinematic-based model halo masses or from using abundance matching.

We fit the evolution of these mass ratios from abundance matching in the form of

$$\left(\frac{M_*}{M_{halo}}\right) = \alpha \times z + \beta.$$

The values of the best-fitting parameters are $\alpha = -0.0016 \pm 0.0006$ and $\beta = 0.011 \pm 0.001$ for galaxies with log $M = 10$, $\alpha = -0.0018 \pm 0.0008$ and $\beta = 0.013 \pm 0.001$ for log $M = 10.3$ systems, $\alpha = -0.0012 \pm 0.0009$ and $\beta = 0.014 \pm 0.001$ for log $M = 10.8$, $\alpha = 0.000045 \pm 0.000008$ and $\beta = 0.011 \pm 0.001$ for log $M = 11$, and $\alpha = 0.0024 \pm 0.0007$ and $\beta = 0.003 \pm 0.001$ for log $M = 11.5$. The only case that has a
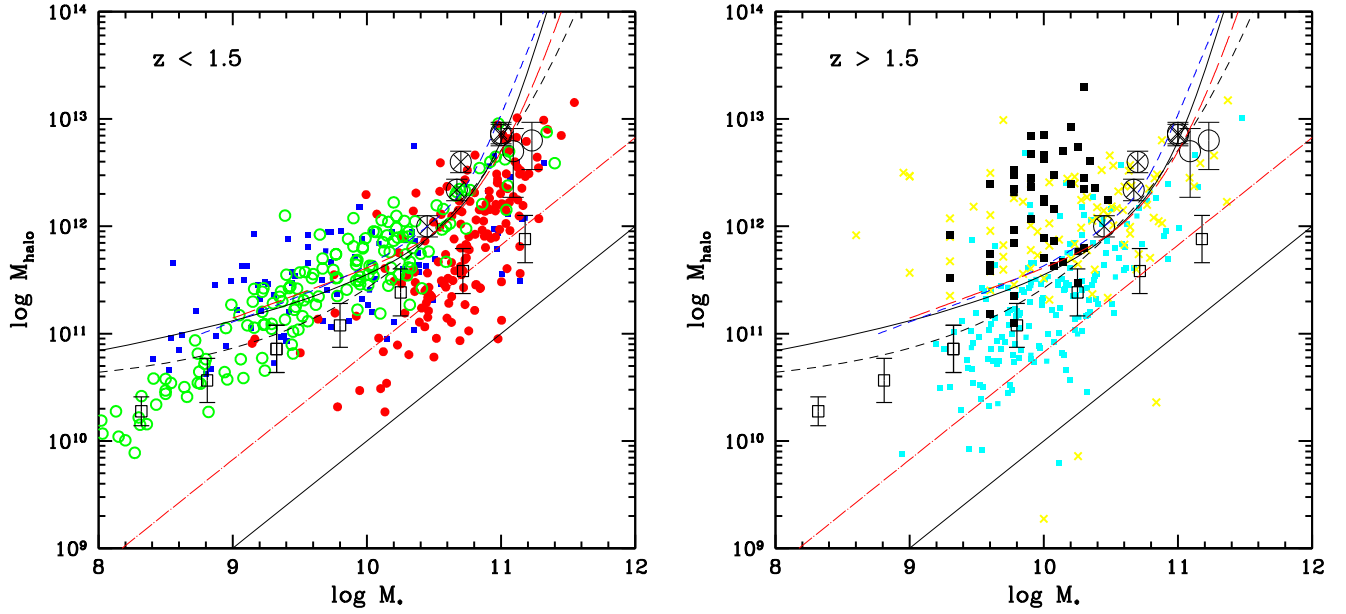
Figure 15. Halo mass as a function of stellar mass computed using various samples and methods. The open squares with error bars show the average and dispersion for the primary sample of galaxies. The large circles at log $M_* \sim 11$ are from the clustering analysis from Foucaud et al. (2010). The large circles with inner crosses are from the clustering measured masses of Skibba et al. (2015). The black solid curved line is the relationship between stellar and halo mass from weak-lensing measurements from van Uitert et al. (2016), the red dashed line is from the lensing results of Leauthaud et al. (2012), and the blue dashed line is from Moster et al. (2013). The black dashed line, just below the red dashed line, is the relationship between stellar and halo mass as derived by the Galacticus simulation. The black solid straight line is the 1:1 relation between the two masses. The other points are data with the same meaning as in Figure 11. The dotted-dashed red line is the baryonic fraction from Planck.

significant slope of $>3\sigma$ is for the highest masses with log $M = 11.5$.

Our results are in agreement with those of Conselice et al. (2005), who also found that the highest-mass galaxies have the highest $M_*/M_{\rm halo}$ ratio. Furthermore, using galaxy clustering, Foucaud et al. (2010) found a declining $M_*/M_{\rm halo}$ ratio with redshift at $z > 1.0$ at a given stellar mass selection. However, Foucaud et al. (2010) effectively measured the parent halo of objects, while we are observing the halo mass for individual "subhalos." Foucaud et al. (2010) interpreted this evolution as a halo downsizing effect.

However, we must keep in mind that the kinematic model mass evolution in the mass ratios is biased. The galaxies toward higher redshifts are more typically star-forming galaxies, with a later-type morphology, and there is no guarantee that these systems are representative of the population as a whole at these redshifts. Our results at $z > 1.5$ should therefore be taken with caution as a preliminary measure of how total and stellar masses relate at higher redshifts.

6. Discussion

6.1. Dark Matter Accretion Rates

These results have implications for the way in which galaxy formation occurs at $z < 3$. With the observation of a nearly constant stellar-to-total mass ratio with redshift, we can derive the accretion rate of both gas and dark matter, building the halos and galaxies over cosmic time. We start off with a method for parameterizing the star formation history, which for our sample can be represented by exponentially declining star formation, such that the SFR as a given redshift $\Psi(z)$ can be written as

$$\Psi(z) = \Psi_0 \times \exp(-t/\tau), \qquad (24)$$

where Ψ_0 is the initial SFR, t is the elapsed time since the SFR began, and τ is the characteristic declining rate of the exponential. This form is a good fit to the stellar populations of galaxies at $z < 3$ (e.g., Mortlock et al. 2013; Ownsworth et al. 2014). Integrating this between two times, t_1 and t_2, we obtain a measure of the amount of stellar mass created between these two epochs:

$$\delta M_* = \tau \times \Psi_0[\exp(-t_1/\tau) - \exp(-t_2/\tau)]. \qquad (25)$$

If we take the SFR to begin at $t_1 = 0$, then this equation reduces to

$$\delta M_* = \tau \times \psi_0[1 - \exp(-t_2/\tau)]. \qquad (26)$$

In what follows, we consider as well the amount of stellar mass that is returned to the ISM of these galaxies after taking into account the results of stellar evolution after 1 Gyr (e.g., Conselice et al. 2013; Ownsworth et al. 2014). If we furthermore consider the form of the ratio of stellar mass to total mass, i.e.,

$$f_{*,\rm halo}(z, M_*) = \frac{M_*(z)}{M_{\rm halo}(z)}, \qquad (27)$$

then a change in stellar mass δM_* corresponds to a change in the total mass given by

$$\delta M_{\rm halo} = \frac{1}{f_{*,\rm halo}} \times \delta M_*, \qquad (28)$$

where we have used the observation that f_* is roughly independent of redshift at $z < 0.5$. Using this, we can then consider how the SFR relates to the change in the stellar mass as given by Equation (26) over a large time period. Between t_1 and t_2, the addition of total mass to the system can be calculated
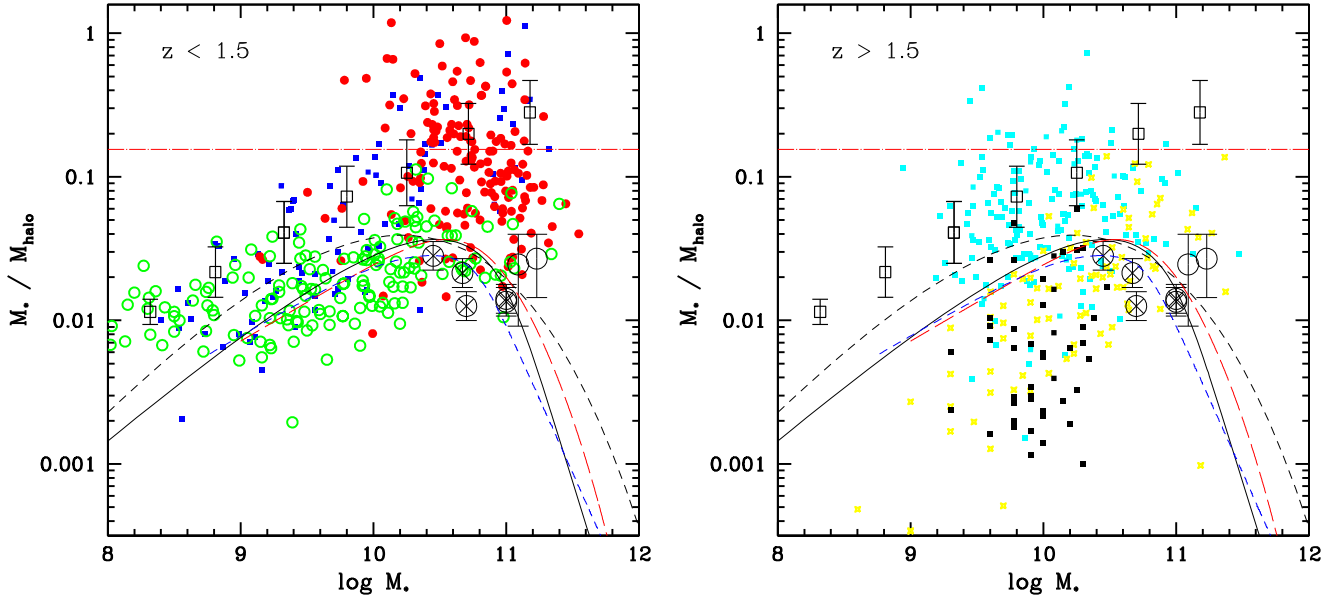
Figure 16. Relationship between stellar mass and halo mass as a function of halo mass with a comparison to previous work. The symbols and lines are the same as those explained in the caption of Figure 15. As can be seen, we do not find a particular peak of galaxy formation efficiency but rather a continual increase at higher stellar masses.
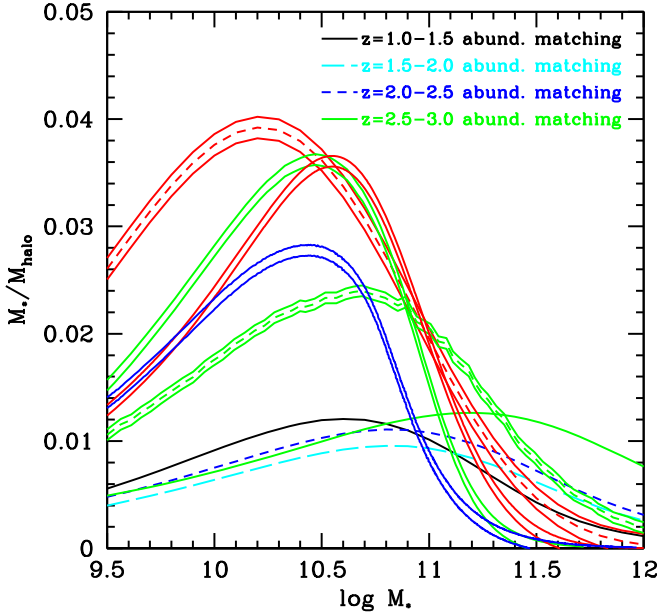

Figure 17. Ratio of stellar to halo mass derived through abundance matching and weak lensing. Shown are four lines from the abundance-matching method representing the relationship between these two quantities from $z = 1$ to 3. The red dashed line surrounded by red solid lines shows the relationship between the halo and stellar masses as derived from the Galacticus simulation. The green double solid line is the relationship between the stellar and halo masses from weak-lensing measurements from van Uitert et al. (2016), the red double solid line is from the lensing results of Leauthaud et al. (2012), and the blue double solid line is from Moster et al. (2013). We also show the abundance-matching stellar and halo masses (green dashed line surrounded by green solid lines) from Conroy & Wechsler (2009).
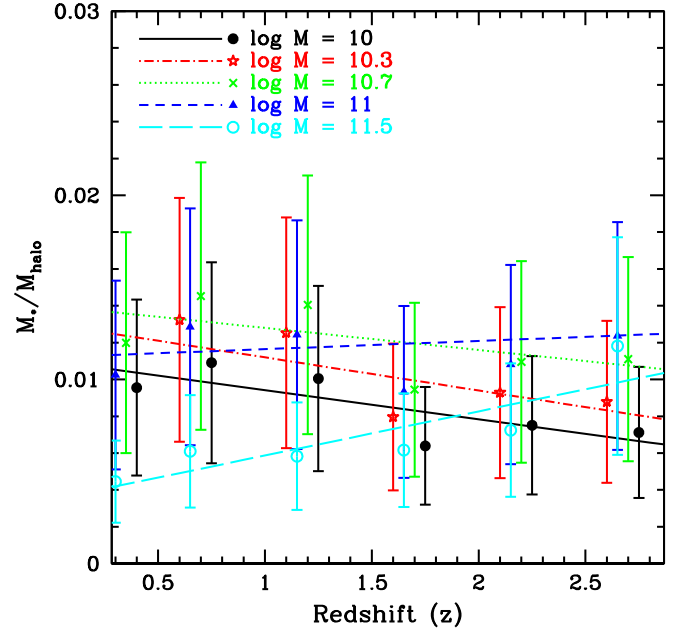

Figure 18. Abundance-matched derived stellar-to-halo mass ratios as a function of redshift. Each line represents a selection in stellar mass. As can be seen, there is very little evolution, and a formula fit suggests that the slopes of these lines are not significantly different from a flat evolution (see text for details).

by combining with Equation (26). We can then write

$$\delta M_{\text{halo}} = \frac{\tau \times \psi_0[1 - \exp(-t_2/\tau)]}{f_*};$$

(29)

however, we can also consider the instantaneous rate of accretion of material in terms of SFR if we use the approximation that $\delta M_* \sim \psi(z)dt$. Using this, we can write the mass accretion rate as

$$\frac{dM_{\text{halo}}(z)}{dt} = \frac{1}{f_*}\psi'(z),$$

(30)

where ψ' is the equivalent SFR after accounting for the amount of mass returned to the ISM through the stellar evolution
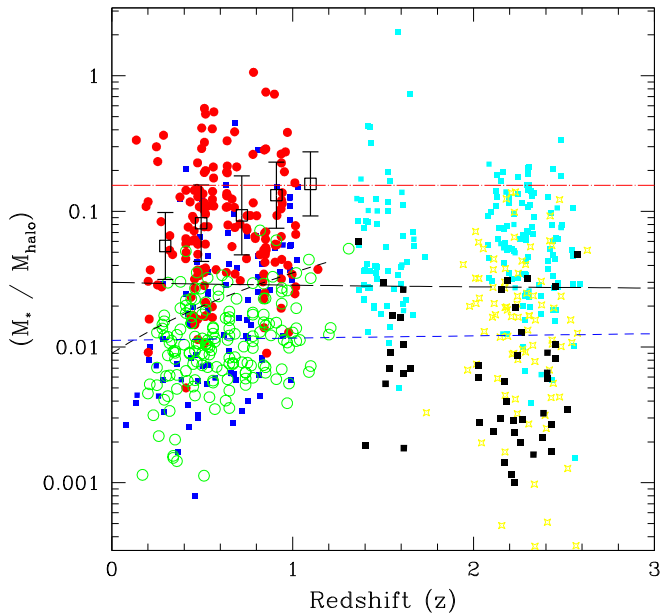
Figure 19. M_*–$M_{\rm halo}$ ratio (f_*) as a function of redshift. The points are the same as in Figure 11. The red horizontal line shows the universal baryonic mass fraction from Planck. We also show the best-fit power laws of the form $f \sim (1 + z)^m$ (see text). The long-dashed line shows this fit to all the data from $z = 0$ to 3, while the short-dashed line shows the fit for the sample at $z < 1.2$, where we find the exponent $m = 1.97$. The blue dashed line shows the relationship between f_* and redshift derived from the abundance matching (see text). The points are otherwise the same as in Figure 11. The red dashed line show the universal baryonic mass to halo mass ratio from *Planck*.

Figure 20. Derived dark matter accretion rate using the relations for stellar and halo masses that we derive in this paper. These are plotted as a function of comoving number density based on the SFR measures from Ownsworth et al. (2014), such that lower number densities correspond to higher stellar masses. As can be seen, rarer massive galaxies have a higher dark matter accretion rate at higher redshifts, but the rate of halo accretion appears to be similar within this mass range. Also plotted as the dashed lines are models for the accretion rate of dark matter based on the theory of Correa et al. (2015), with total masses for each model labeled.

processes. Effectively, this is the stellar mass formation rate, rather than just the SFR. Through the use of stellar evolution models, the effective stellar mass formation rate is around 70% of the SFR after a few Gyr.

From Ownsworth et al. (2014), we know how the SFR of galaxies with similar masses to those studied here evolves. Overall, the SFR is given by the form in Equation (24), with $\psi_0 = 135\,M_\odot\,{\rm yr}^{-1}$ and $\tau = 2.4 \times 10^9$ yr. Furthermore, the observed SFRs are $\psi = 55\,M_\odot\,{\rm yr}^{-1}$ at $z = 3$, $\psi = 34\,M_\odot\,{\rm yr}^{-1}$ at $z = 2$, and $\psi = 12\,M_\odot\,{\rm yr}^{-1}$ at $z = 1$.

Using the value of $f_{*,\rm halo}$ given in Section 5 and Equation (30), we calculate the total mass accretion rate. We show these calculated values as a function of mass and redshift in Figure 20. This figure reveals that the total mass accretion rate for typical galaxies varies with stellar mass and redshift. We find that the peak halo accretion rate is around $\dot{M}_{\rm halo} \sim 4000\,M_\odot\,{\rm yr}^{-1}$ at $z \sim 2.5$. This is much higher than the stellar mass or gas accretion rates at similar redshifts (e.g., Conselice et al. 2013; Mortlock et al. 2015; Ownsworth et al. 2014).

We find that within our assumptions, galaxies grow their total integrated halo mass $M_{\rm halo}$ at a self-similar rate as their stellar M_* masses. The M_* growth can be explained by the process of mergers (both major and minor) triggering star formation events, which increases M_*. The gas for this must come from both minor/major mergers and gas accretion (e.g., Conselice et al. 2013; Mundy et al. 2017). The fact that the dark matter accretion rate follows that of the SFR, revealing a nearly constant ratio at $z > 1$, implies that the dark matter is being accreted with the baryons in these galaxies to build up the mass of the system at this epoch.
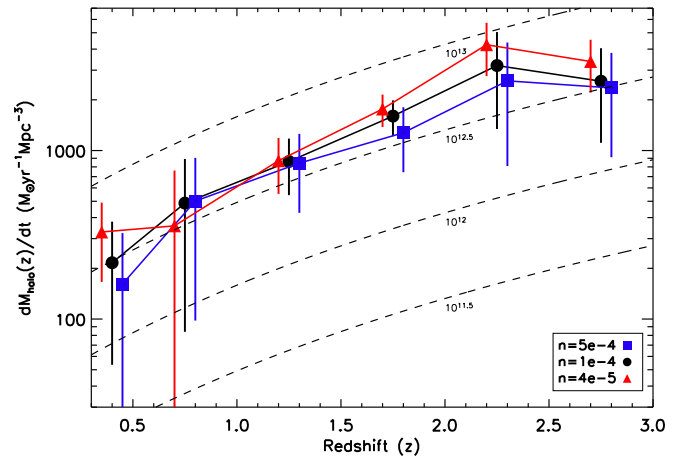
We can also compare these values to theory, which predicts, even based on analytical calculations, what the accretion rate of dark matter onto halos is (e.g., van den Bosch 2002; Wechsler et al. 2002; McBride et al. 2009; Correa et al. 2015). For example, Wechsler et al. (2002) predicted an accretion history that scales as an exponential: $M \sim e^{-\alpha z}$.

It is proposed based on these various simulations and calculations using the extended Press–Schechter (EPS) formalism that the total mass accretion history can be represented by a combination of an exponential and a power law in the form (e.g., McBride et al. 2009; Correa et al. 2015)

$$M(z) = M_0 \times (1 + z)^\alpha \times e^{\beta \times z}. \tag{31}$$

Taking the derivative of this, we find that the rate of change of the halo mass is given by (e.g., Correa et al. 2015)

$$\frac{dM}{dt} = 71.6\,M_\odot\,{\rm yr}^{-1}\,M_{12}$$
$$\times\,[-\alpha - \beta(1 + z)][\Omega_m(1 + z)^3 + \Omega_\Lambda]^{1/2}, \tag{32}$$

where M_{12} is the halo mass of the galaxy in units of $10^{12}\,M_\odot$, and Ω_m and Ω_λ are the cosmology.

When we fit our data and observations to this, we find that the values of α and β are as given in Table 10. This is in agreement with our observations, as can be seen in the comparison in Figure 20. This is similar to the results of the mass accretion rates derived from other, similar assumptions (e.g., Behroozi et al. 2013; Rodríguez-Puebla et al. 2017).

6.2. Dark Matter Mass as a Regulator of Galaxy Formation

One of the goals in this paper is to relate the matter components of galaxies beyond the local universe and develop a method for doing it that can be applied to single galaxies as opposed to stacked systems, as used in clustering and lensing (e.g., Coupon et al. 2015). In general, we find that the stellar mass is, within some scatter, a good tracer of the dynamical mass and halo masses of field galaxies at $z < 1.2$ within our mass range. This may not be the case for red passive

Table 10
The Values of α and β for Galaxies Selected at Different Number Densities
(See Ownsworth et al. 2014)

Density (Mpc^{-3})	log M_*	log M_{halo}	α	β
5×10^{-4}	10.8	12.4	-0.44 ± 1.25	-0.88 ± 0.41
1×10^{-4}	11.2	13.1	-0.12 ± 0.37	-0.20 ± 0.11
4×10^{-5}	11.4	13.3	0.07 ± 0.33	0.21 ± 0.11

Note. These values give the form for the growth of halos at the given mass limit and are consistent with the theoretical work of Correa et al. (2015).

galaxies or those in very dense areas such as clusters, which are not present in our sample in great abundance.

This suggests that the different masses in galaxies and how they build up over time are highly regulated by the overall halo mass of the galaxy, which drives the formation of the amount of stellar mass within these galaxies. That is, fundamentally, the formation of galaxies is hierarchical, with dark matter accreted from the IGM the main way mass is built up. When this dark matter is accreted, baryonic mass is as well, which leads to additional galaxy formation processes such as star formation and likely AGN activity. This also suggests that galaxies are assembling hierarchically, independent of the method in which mass is brought into the systems, whether it be through mergers of various types or through, e.g., gas accretion processes.

This is similar to previous findings from other papers, including Kravtsov et al. (2018), where the masses of the brightest cluster galaxies (BCGs) have a stellar mass that scales with total mass (M_{500}) such that $M_{*,\mathrm{BCG}} \sim M_{500}^{0.4}$, with a scatter in M_{500} of 0.2 dex for centrals. Satellite galaxies within this sample have scaling that goes as $M_{*,\mathrm{sat}} \sim M_{500}^{0.8}$, with a smaller scatter of 0.1 dex. This is similar to our results when we examine the scaling between the stellar mass and halo mass for our systems (Section 5.1.2).

6.3. Galaxy Formation Efficiency

A standard way to characterize the efficiency of galaxy formation is to compare the stellar masses of galaxies to their halo masses and find where this ratio peaks as a function of stellar mass and redshift. Furthermore, it is interesting to determine if this peak changes as a function of redshift, as well as if different methods give different answers to this observational question.

It is well known that the peak of the galaxy formation efficiency, i.e., when the stellar to dark matter masses has its highest value, is at roughly log $M_* = 10.5$ or log $M_{\mathrm{halo}} \sim 12$ (e.g., Behroozi et al. 2013) through the use of abundance matching. Our results show a few things that are worth discussing in detail and following up, as we do not find such clear-cut evidence for a turnover, at least to within the mass limits of our sample.

First, we find that the ratio of stellar mass to halo mass declines as we observe galaxies at lower stellar masses at $z < 1.5$. This is as expected and shows that the galaxy formation process efficiency is lower for lower-mass galaxies, as seen in the comparison points from abundance matching and lensing as shown in Figure 16. However, we do not find a "peak" in the galaxy formation process, as we find a continual increase in the ratio of stellar to halo mass for individual galaxies as we go to higher masses. This suggests that the dark

matter masses we are measuring are only for single galaxies and not large halo masses, as what might be measured in groups or clusters of galaxies. Our samples are generally not taken from dense environments, and this may be one reason we do not see an enlarged halo mass for the highest-mass galaxies.

There is also the issue that the peak in the galaxy formation may evolve with redshift, as is found in halo clustering–derived masses (e.g., Coupon et al. 2012). However, this is likely due to the fact that the halo masses derived with clustering measures are observing more of the massive parent halo masses due to halo downsizing. We do not see any evidence for evolution in the ratio of stellar to halo mass, nor do we see evidence that the galaxy formation efficiency peak is changing at higher redshifts.

Based on current ideas, we would expect the stellar mass–to–halo mass ratios for the most massive galaxies to decline from a peak at the highest masses. We would see this as the most massive galaxies having the largest relative dark matter content. This is usually interpreted as being due to AGN feedback, which is most effective at the highest stellar and halo masses, thus preventing gas from cooling to form stars. The fact that we do not see this, at least when we compare this ratio with stellar mass, suggests that halo masses for these very massive galaxies we are measuring are for the halo associated with just the galaxy itself, not the overall larger halo that might be present. This may alternatively imply that the effects of AGN feedback are not important for determining the total amount of baryonic mass formed or that the effects are most pronounced in the outer parts of halos.

In fact, the greatest effect we see is a form of halo downsizing, whereby the earliest galaxies to form in the "oldest" halos have the largest stellar mass to dark matter mass. This implies that the time these halos form is more critical for their overall "efficiency" of galaxy formation than any other process. We can see this with a higher stellar mass–to–halo mass ratio at a given mass for systems that are ellipticals compared with, for example, disks. This higher stellar-to-halo mass ratio is also seen in the models, suggesting that the time of formation is indeed the third parameter in the correlation between the stellar mass and halo masses of galaxies, which correlates with the dynamical mass (Section 4.3).

7. Conclusions and Summary

In this paper, we examine the different forms of galaxy mass (stellar, dynamical, halo) at high redshifts from $z = 0.4$ to 3. We take as our starting point a well-defined sample of 544 galaxies with well-measured SFRs, kinematics, and sizes and derive relations between the derived stellar masses, dynamical masses, and halo masses. We find the following major results.

1. Galaxy halo and dynamical masses can be successfully retrieved used the $S_{0.5}$ index, which combines the use of a galaxy's velocity dispersion and its rotational velocity. This is superior to using just a velocity dispersion or rotational velocity and allows the measurement of halo masses on individual systems as opposed to ensemble averages. We furthermore argue that the third parameter in this fit is the time of halo formation, with systems forming earlier having a higher stellar-to-halo mass ratio.

1. There is a strong relation between the stellar and dynamical masses for galaxies that occupy their own massive halos (i.e., field galaxies). This suggests that
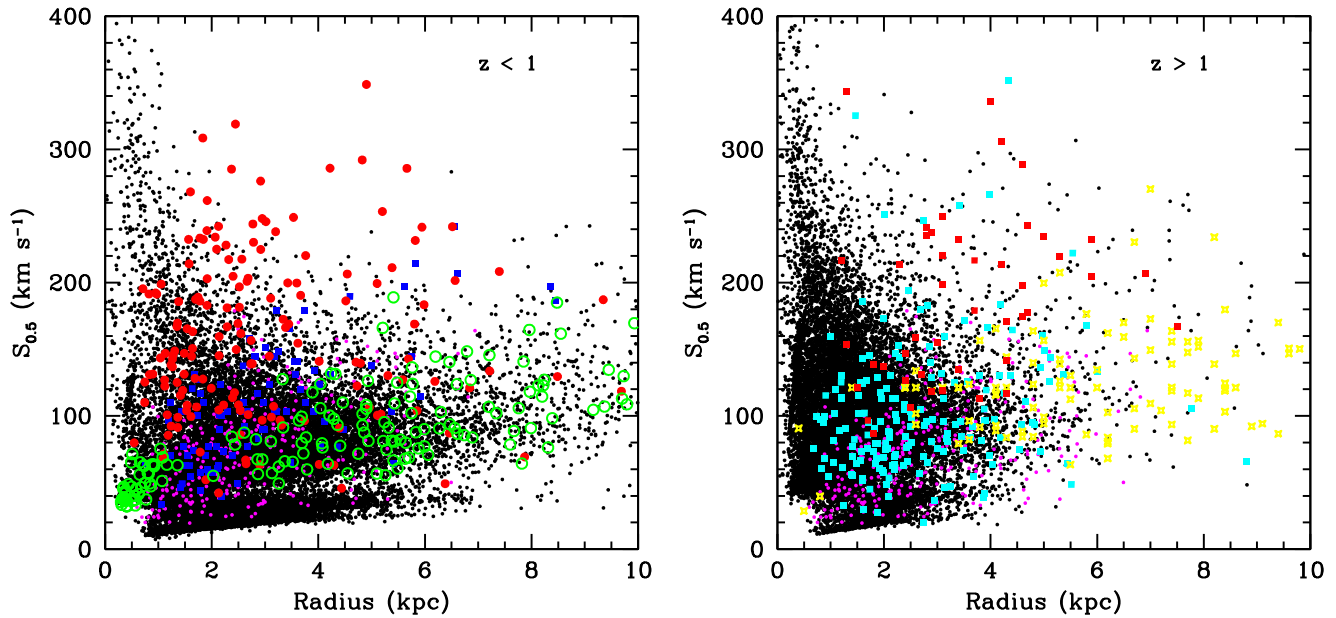
Figure 21. Relationship between the $S_{0.5}$ parameter and the sizes of galaxies, both of which go into calculating the dynamical masses. The small black points are from the Galacticus simulation, while the remaining points are the same as in Figure 11.

galaxy formation is highly regulated and the different masses are correlated and assembled together in galaxies.

2. We show that within the visible radius, the dynamical masses of the galaxies in our sample are dominated by stellar mass up to $z = 1.2$.

3. We derive the halo masses of galaxies by using semi-analytical models that show how to relate the internal velocities, size, and halo mass together. This method shows that the most massive galaxies in stars have the highest ratios of stellar to halo mass, while the least massive galaxies have the lowest ratios.

4. We develop a series of empirically based relations between the stellar masses of galaxies and their dark masses as a function of redshift. The scatter in these relations is just slightly higher than the expected error budget in stellar masses, with a dispersion of around $\sim$0.3 dex.

5. We use the fact that the stellar to halo mass does not appear to change significantly with redshift at $z > 1$ to argue that the dark matter accretion rate is $\dot{M}_{\rm halo} \sim$ 4000 $M_{\odot}\,{\rm yr}^{-1}$ at $z \sim 2.5$ down to an accretion rate of a few hundred $M_{\odot}\,{\rm yr}^{-1}$ by $z \sim 0.5$.

In the future, these types of observations can be extended, with longer exposures obtaining deeper kinematic data in the outer parts of galaxies that will hopefully give us a better and more accurate idea of the halo masses for these systems. Doing this is, however, very difficult with current technology and may require the use of spectrographs on 20–30 m telescopes in the next decade. In the meantime, clustering and lensing analyses of masses will make headway in terms of average galaxy properties, and we can measure the mass evolution for bulk galaxies divided into finer subsets.

Appendix A
The Meaning and Usefulness of the $S_{0.5}$ Parameter

As mentioned in the body of the paper, we use the $S_{0.5}$ parameter (Section 3.2) throughout to derive the dynamical masses of galaxies; furthermore, we use this measurement as a proxy and a way to obtain the halo masses of a galaxy. We investigate in this appendix the nature of the $S_{0.5}$ parameter and how to interpret the resulting dynamical mass calculated from it.

First, we determine how the distribution of $S_{0.5}$ values in the models matches the data. To do this, we compare at both $z < 1$ and $z > 1$ the distribution of half-light radii and $S_{0.5}$ values. As shown in Figure 21, there is a good overlap in these values; i.e., the simulation we use to calculate the dynamical masses has a good overlap with the actual data at both high and low redshift. This is also the case when comparing with the observed and predicted relation between $S_{0.5}$ and stellar mass (Figure 10; Section 5.1.1) in a TFR-like relation.

The one exception to this is that we observationally do not see high internal velocity systems that have very small radii in the same abundance as the simulations. We do, however, find that there are galaxies with larger radii, namely the early types, which have large $S_{0.5}$ parameters but are not abundant in the model itself. We therefore exclude these simulated galaxies in our further analyses that have sizes >10 kpc. We also find systems that have a very small radius and large value of combined velocities through the $S_{0.5}$ parameter that we also exclude from our analyses.
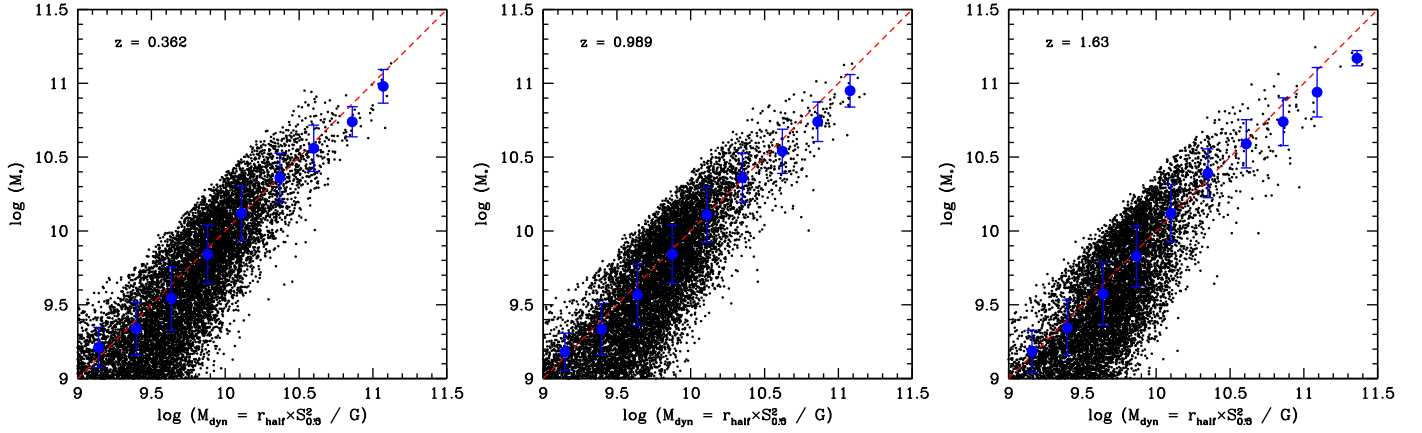
Figure 22. Relationship between dynamical mass and stellar mass, with the dynamical mass defined using the $S_{0.5}$ parameter as in Equation (2). The dashed red line shows the 1:1 relation between these two quantities, and the blue points with error bars show the average values at different masses and the scatter within that dynamical mass bin.

The nature of dynamical masses from $S_{0.5}$ is such that it should represent a good indicator for the total mass within the galaxy itself, or it correlates in some way with the total amount of mass within the galaxy. Thus, within the brighter portion of a galaxy, within R_e, we would expect that the total mass of our galaxies is dominated by the stellar mass, as dark matter would have very little expected contribution to the inner portions of galaxies.

To demonstrate how good this assumption is, we plot at three different redshifts the relationship between the dynamical mass and the stellar mass in Figure 22. Here the dynamical mass is measured at exactly the half-light radius; thus, we do not implement the β term from Equation (3) here.

As can be seen, there is a good relationship between the stellar mass and dynamical mass within the Galacticus models. This relationship is nearly 1:1 up to about stellar masses of $M_* = 10^{11}\,M_\odot$, when the relationship becomes softer, particularly at higher dynamical masses at a lower redshift. However, this difference is less striking at higher redshifts, $z = 1.63$, where the relationship between these two quantities is slightly improved. This figure, however, does justify the use of our dynamical mass as a measure of "mass" in a galaxy. Given that it is kinematically based and measured within the visible portions of galaxies, we find that it statically matches the stellar mass at the location where the stellar mass dominates the total mass of a galaxy.

Appendix B
Other Fitting Forms

B.1. Modeled Stellar Mass–to–Halo Mass Relation

There are a myriad of ways that the relation between the stellar mass or dynamical mass can be fit as a function of the halo mass. In this section, we discuss some of these fits and give their forms. We also consider how other masses, the circular mass and the σ mass, are related to the halo mass. First, however, we consider alternative methods for measuring the halo mass based on the dynamical mass.

The first relationship we consider is whereby the relation between stellar and halo mass is fit by two power laws with a break at $M_* \sim 10^{9.9}\,M_\odot$, which is the representative location where the slope of the relationship changes. We fit this relation between stellar and halo mass with a linear relationship

between the log of these quantities using the form

$$\log M_{\rm halo} = \alpha \times \log M_* + \beta, \qquad (33)$$

where the quantities for α and β are listed in Table 11 at the separation point $\log M_* = 9.5$. As we find in the main paper, we find that there is no evolution in the relationship between stellar and halo masses, at least in these models.

We also examine results from the Millennium simulation to see if there is any difference between different models for the relationship between stellar and halo mass. To carry out this comparison, we select galaxies from the De Lucia & Blaizot (2007) catalog at $z \sim 1$, giving us 684,357 galaxies selecting both stellar and halo masses. We use the friend-of-friend halo masses from this simulation as a measure of our halo mass. These friends-of-friends masses are not based on a certain mass threshold but on a linking length parameter, and there is a variation in the mass overdensity depending upon the concentration of the various mass profiles (e.g., More et al. 2011). The corresponding relationship for the Millennium simulation over our redshifts of interest is given by

$$\log M_{\rm halo} = (0.584 \pm 0.029) \log (M_*) + (5.556 \pm 0.271)$$
$$M_* < 10^{9.9}$$
$$\log M_{\rm halo} = (1.442 \pm 0.060) \log (M_*) - (3.107 \pm 0.616).$$
$$M_* \geqslant 10^{9.9}.$$
$$(34)$$

We find a very similar relationship to what we find in the Galacticus simulations, which we discuss in the main body of the paper.

B.2. Alternative Dynamical Mass–Halo Mass Relations

B.2.1. Moster et al. (2010) Functional Form

One of the functional forms in which we fit the dynamical to halo mass is that established by Moster et al. (2010) for the relationship between the stellar mass and the halo mass through abundance matching. The form of this fitting for our relation

Table 11
The Fitted Values of α and β for the Relation between Stellar and Halo Mass as Found through the Galacticus Simulation

Redshift	$\log M_* < 9.9$		$\log M_* > 9.9$	
	α	β	α	β
0.4	0.44 ± 0.04	6.8 ± 0.3	1.68 ± 0.12	-5.8 ± 1.3
0.7	0.38 ± 0.05	7.5 ± 0.4	1.65 ± 0.05	-5.5 ± 0.6
1.0	0.40 ± 0.05	7.2 ± 0.4	1.65 ± 0.04	-5.4 ± 0.5
1.3	0.44 ± 0.05	6.9 ± 0.5	1.58 ± 0.02	-4.7 ± 0.2
1.6	0.44 ± 0.05	6.9 ± 0.4	1.55 ± 0.02	-4.2 ± 0.1
1.9	0.42 ± 0.04	7.1 ± 0.4	1.53 ± 0.04	-4.0 ± 0.4

Note. These values are used in Equation (33).

between the dynamical and halo masses is

$$\log M_{\rm halo} = 2 \times (\log M_{\rm halo})_0 \left[\left(\frac{\log M_*}{M_1} \right)^{-\beta} + \left(\frac{\log M_*}{M_1} \right)^{\Gamma} \right]. \tag{35}$$

As discussed in Section 4.3, the best-fitting relations for the Moster et al. (2010) relations are shown as the green line in Figure 5. As also discussed, these fits are not superior to the simplified form of a single power-law relationship between the value of $\log M_{\rm dyn}$ and $\log M_{\rm halo}$. We also use this form of fit when fitting the σ mass to the halo mass in Section 4.3.3 and Figure 7. It is likely that this more complex form is more accurate for fitting functional forms, something that can be explored in more detail once models predicting the quantities we study are better calibrated.

ORCID iDs

Christopher J. Conselice ● https://orcid.org/0000-0003-1949-7638

References

Agertz, O., & Kravtsov, A. V. 2016, ApJ, 824, 79
Bauer, A. E., Conselice, C. J., Pérez-González, P. G., et al. 2011, MNRAS, 417, 289
Behroozi, P. S., Wechsler, R. H., & Conroy, C. 2013, ApJ, 770, 57
Beifiori, A., et al. 2014, ApJ, 789, 92
Bell, E. F., McIntosh, D. H., Katz, N., & Weinberg, M. D. 2003, ApJS, 149, 289
Benson, A. J. 2012, NewA, 17, 175
Benson, A. J. 2014, MNRAS, 444, 2599
Berlind, A. A., et al. 2003, ApJ, 593, 1
Binney, J., & Tremaine, S. 1987, (Princeton, NJ: Princeton Univ. Press), 747
Bonnet, H., Abuter, R., Baker, A., et al. 2004, Msngr, 117, 17
Bruzual, G., & Charlot, S. 2003, MNRAS, 344, 1000
Bryan, G. L., & Norman, M. L. 1998, ApJ, 495, 80
Buchan, S., & Shankar, F. 2016, MNRAS, 462, 2001
Buitrago, F., Trujillo, I., Conselice, C. J., & Häußler, B. 2013, MNRAS, 428, 1460
Bundy, K., Ellis, R. S., Conselice, C. J., et al. 2006, ApJ, 651, 120
Cappellari, M., Bacon, R., Bureau, M., et al. 2006, MNRAS, 366, 1126
Cappellari, et al. 2013, MNRAS, 432, 1709
Chabrier, G. 2003, PASP, 115, 763
Conroy, C., Prada, F., Newman, J, et al. 2007, ApJ, 654, 153
Conroy, C., & Wechsler, R. H. 2009, ApJ, 696, 620
Conroy, C., Wechsler, R. H., & Kravtsov, A. V. 2006, ApJ, 647, 201
Conselice, C. J. 2003, ApJS, 147, 1
Conselice, C. J. 2014, ARA&A, 52, 291
Conselice, C. J., Bundy, K., Ellis, R. S., et al. 2005, ApJ, 628, 160
Conselice, C. J., Bundy, K., Trujillo, I., et al. 2007, MNRAS, 381, 962

Conselice, C. J., Bundy, K., Vivian, U., et al. 2008a, MNRAS, 383, 1366
Conselice, C. J., Mortlock, A., Bluck, A. F. L., Grützbauch, R., & Duncan, K. 2013, MNRAS, 430, 1051
Conselice, C. J., Rajgor, S., & Myers, R. 2008b, MNRAS, 386, 909
Correa, C. A., Wyithe, J. S. B., Schaye, J., & Duffy, A. R. 2015, MNRAS, 450, 1514
Cattaneo, A., Salucci, P., & Papastergis, E. 2014, ApJ, 783, 66
Coupon, J., et al. 2012, A&A, 542, 5
Coupon, J., Arnouts, S., van Waerbeke, L., et al. 2015, MNRAS, 449, 1352
Davis, M., Efstathiou, G., Frenk, C. S., & White, S. D. M. 1985, ApJ, 292, 371
Davis, M., Faber, S. M., Newman, J., et al. 2003, Proc. SPIE, 4834, 161
Davis, M., Guhathakurta, P., Konidaris, N. P., et al. 2007, ApJL, 660, L1
De Lucia, G., & Blaizot, J. 2007, MNRAS, 375, 2
Drory, N., Salvato, M., Gabasch, A., et al. 2005, ApJL, 619, L131
Duncan, K., Conselice, C. J., Mortlock, A., et al. 2014, MNRAS, 444, 2960
Eisenhauer, F., Abuter, R., Bickert, K., et al. 2003, Proc. SPIE, 4841, 1548
Eisenstein, D. J., & Hu, W. 1998, ApJ, 496, 605
Elsner, F., Feulner, G., & Hopp, U. 2008, A&A, 477, 503
Epinat, B., Contini, T., Le Fvre, O., et al. 2009, A&A, 504, 789
Erb, D. K., Steidel, C. C., Shapely, A. E., et al. 2006, ApJ, 646, 107
Faber, S. M., & Gallagher, J. S. 1979, ARA&A, 17, 135
Förster Schreiber, N. M., Genzel, R., Bouché, N., et al. 2009, ApJ, 706, 1364
Förster Schreiber, N. M., Genzel, R., Lehnert, M. D., et al. 2006, ApJ, 645, 1062
Foucaud, S., Conselice, C. J., Hartley, W. G., et al. 2010, MNRAS, 406, 147
Guerou, A., Krajnović, D., Epinat, B., et al. 2017, A&A, 608, A5
Hartley, W. G., Conselice, C. J., Mortlock, A., Foucaud, S., & Simpson, C. 2015, MNRAS, 451, 1613
Hearin, A. P., & Watson, D. F. 2013, MNRAS, 435, 1313
Hearin, A. P., Watson, D. F., & van den Bosch, F. C. 2015, MNRAS, 452, 1958
Hearin, A. P., Zentner, A. R., Berlind, A. A., & Newman, J. A. 2013, MNRAS, 433, 659
Hopkins, P. F., Croton, D., Bundy, K., et al. 2010, ApJ, 724, 915
Ilbert, O., et al. 2013, A&A, 556, 55
Jenkins, A., Frenk, C. S., White, S. D. M., et al. 2001, MNRAS, 321, 372
Kassin, S. A., Weiner, B. J., & Faber, S. M. 2007, ApJL, 660, L35
Kauffmann, G., Li, C., Zhang, W., & Weinmann, S. 2013, MNRAS, 430, 1447
Kobulnicky, H. A., & Gebhardt, K. 2000, AJ, 119, 1608
Kravtsov, A. V. 2013, ApJL, 764, L31
Kravtsov, A. V., Berlind, A. A., Wechsler, R. H., et al. 2004, ApJ, 609, 35
Kravtsov, A. V., Vikhlinin, A., & Meshscheryakov, A. 2018, AstL, 44, 8
Kriek, M., Shapley, A. E., Reddy, N. A., et al. 2015, ApJS, 218, 15
Lampichler, N., Maier, C., & Ziegler, B. 2017, arXiv:1707.09838
Lanyon-Foster, N. M., Conselice, C. J., & Merrifield, M. 2012, MNRAS, 424, 1852
Leauthaud, A., et al. 2012
McBride, J., Fakhouri, O., & Ma, C.-P. 2009, MNRAS, 398, 1858
McCracken, H. J., Wolk, M., Colombi, S., et al. 2015, MNRAS, 449, 901
Miller, S. H., Bundy, K., Sullivan, M., Ellis, R. S., & Treu, T. 2011, ApJ, 741, 115
Miller, S. H., Ellis, R. S., Newman, A. B., & Benson, A. 2014, ApJ, 782, 115
More, S., Kravtsov, A., Dalal, N., & Gottlober, S. 2011, ApJS, 195, 4
Mortlock, A., Conselice, C. J., Bluck, A. F. L., et al. 2011, MNRAS, 413, 2845
Mortlock, A., Conselice, C. J., Hartley, W. G., et al. 2015, MNRAS, 447, 2
Mortlock, A., et al. 2013, MNRAS, 433, 1185
Moster, B., Naab, T., & White, S. D. M. 2013, MNRAS, 428, 3121
Moster, B. P., Somerville, R. S., Maulbetsch, C., et al. 2010, ApJ, 710, 903
Mundy, C. J., Conselice, C. J., Duncan, K. J., et al. 2017, MNRAS, 470, 3507
Muzzin, A., et al. 2013, ApJ, 777, 18
Navarro, J. F., Frenk, C. S., & White, S. D. M. 1996, ApJ, 462, 563
Noeske, K. G., Faber, S. M., Weiner, B. J., et al. 2007, ApJL, 660, L47
Ownsworth, J. R., Conselice, C. J., Mortlock, A., et al. 2014, MNRAS, 445, 2198
Pasquini, L., Avila, G., Blecha, A., et al. 2002, Msngr, 110, 1
Pérez-González, P. G., Rieke, G. H., Villar, V., et al. 2008, ApJ, 675, 234
Persic, M., Salucci, P., & Stel, F. 1996, MNRAS, 281, 27
Price, S., et al. 2016, ApJ, 819, 80
Rodríguez-Puebla, A., Avila-Reese, V., Yang, X., et al. 2015, ApJ, 799, 130
Rodríguez-Puebla, A., Primack, J. R., Avila-Reese, V., & Faber, S. M. 2017, MNRAS, 470, 651
Schiminovich, D., Wyder, T. K., Martin, D. C., et al. 2007, ApJS, 173, 315
Seljak, U. 2000, MNRAS, 318, 203

Shankar, F., Lapi, A., Salucci, P., De Zotti, G., & Danese, L. 2006, ApJ, 643, 14
Shankar, F., et al. 2014, ApJ, 797, 27L
Sheth, R. K., & Tormen, G. 1999, MNRAS, 308, 119
Skibba, R., et al. 2015, ApJ, 807, 152
Springel, V., et al. 2005, Nat, 435, 629
Tiley, A. L., Stott, J. P., Swinbank, A. M., et al. 2016, MNRAS, 460, 103
Treu, T., Ellis, R. S., Liao, T. X., et al. 2005, ApJ, 633, 174
Trujillo, I., Conselice, C. J., Bundy, K., et al. 2007, MNRAS, 382, 109
Twite, J. W., Conselice, C. J., Buitrago, F., et al. 2012, MNRAS, 420, 1061
Ubler, H., et al. 2017, ApJ, 842, 121

van den Bosch, F. C. 2002, MNRAS, 331, 98
van Uitert, E., et al. 2016, MNRAS, 459, 3251
Wake, D. A., Whitaker, K. E., Labbé, I., et al. 2011, ApJ, 728, 46
Wechsler, R. H., Bullock, J. S., Primack, J. R., Kravtsov, A. V., & Dekel, A. 2002, ApJ, 568, 52
Weiner, B. J., Willmer, C. N. A., Faber, S. M., et al. 2006, ApJ, 653, 1027
Weinmann, S. M., van den Bosch, F. C., Yang, X., & Mo, H. J. 2006, MNRAS, 366, 2
White, S. D. M., & Rees, M. 1978, MNRAS, 183, 341
Wisnioski, E., Förster Schreiber, N. M., Wuyts, S., et al. 2015, ApJ, 799, 209
Wuyts, S., Förster Schreiber, N. M., Wisnioski, E., et al. 2016, ApJ, 831, 149